Observed modulation of wintertime Western Arctic mixed-phase cloud properties by sea ice conditions, their long-term variabilities and trends

Pablo Saavedra Garfias[1,2] and Heike Kalesse-Los[1]

[1]Institute for Meteorology, Faculty of Physics and Earth System Sciences, Leipzig University, Leipzig, Germany.
[2]Leibniz Institute for Atmospheric Physics at the University of Rostock, Kühlungsborn, Germany.

Correspondence: P. Saavedra Garfias (pablo.saavedra@uni-leipzig.de)

Abstract. To assess the long-term interaction between sea ice conditions and Arctic mixed-phase cloud (MPC) properties, fourteen winter seasons of observations from the North Slope of Alaska are analysed. MPC properties are set into context with sea ice conditions by determining the sea ice sectors which are most relevant to interact with the observed clouds. A conical sector of 6° and 50 km radius of upstream sea ice concentration (SIC) is considered based on the azimuth direction of the maximum water vapour transport (WVT) within the atmospheric boundary layer. The WVT height is used as indicator ~~for the WVT interacting~~ of its interaction with the cloud, ~~which is categorized as~~ allowing it to be classified as either cloud-coupled or decoupled. The MPC properties are classified according to the presence of high or low pressure systems and analysed as a function of SIC. Results highlight which MPC properties ~~do increase in magnitude~~ significantly change as SIC decreases. The long-term time series evolution shows positive and negative trends in MPC properties, depending on the WVT coupling status and the atmospheric pressure system. The study ~~found~~ finds statistically significant positive trends suggesting an increase of sea ice-MPC coupled liquid water path (+35.0±0.9 $\mathrm{g\,m^{-2}\,decade^{-1}}$), cloud base height (+44.0±0.7 $\mathrm{m\,decade^{-1}}$) and cloud top temperature (+2.2±0.7 $\mathrm{K\,decade^{-1}}$) under low pressure weather systems. It ~~has been~~ is also revealed that the evolution of MPC properties presents cyclical characteristics and it is hypothesized that those are in phase with climate oscillations like ENSO or PDO. Although the results support this hypothesis, a direct causation is not trivial.

Copyright statement. TEXT

1 Introduction

Climate physics has long ago established that increases in atmospheric concentrations of greenhouse gases warms the atmosphere (Arrhenius, 1897; Hegerl, 2022). Observations in recent decades have suggested that the Arctic is warming two to four times faster than the whole Earth ~~(Rantanen et al., 2022; Wendisch et al., 2023)~~(Rantanen et al., 2022; Wendisch et al., 2023; Tan et al., 20
, a phenomenon known as Arctic amplification (AA) (Serreze and Francis, 2006; Serreze and Barry, 2011). Studies have shown that AA in climate models is related to the response to external forcings, primarily the atmospheric lapse-rate feedback as well

as sea ice related feedbacks. However, the lack of full consensus on the magnitude of AA is attributed to the failure to simulate the sensitivity of Arctic sea ice loss to the rise of global temperature (Notz and Community, 2020; Rantanen et al., 2022).

During Polar night, Arctic mixed-phase clouds have a positive cloud radiative effect (CRE), which foster the warming of the surface beneath (Shupe and Intrieri, 2004; Cox et al., 2015). The CRE feedback mechanism contributes to AA and to sea ice decline. The magnitude of this forcing depends on micro- and macro-physical cloud properties (Shupe and Intrieri, 2004; Tan and Storelvmo, 2019). Extensive efforts are currently being performed to improve the understanding of the role MPCs in a changing Arctic ~~(Morrison et al., 2012; Korolev and Milbrandt, 2022)~~ (Morrison et al., 2012; Korolev and Milbrandt, 2022; Tan et al., 2023) as well as to improve their representation in weather and climate models (Schemann and Ebell, 2020; Hofer et al., 2024; Tan et al., 2025). Recently, Cesana et al. (2025), albeit focused on Antarctica, found that prescribing winds in climate models improves the modeled variability of sea ice and clouds compared to satellite observations. They further pointed out that a realistic representation of clouds is crucial to capture the observed sea ice trends that climate models struggle to reproduce. Large scale Pan-Arctic studies have highlighted contrasting differences between clouds located above sea ice or open water: Palm et al. (2010) reported that areas with little or no sea ice are correlated with more cloudiness and a higher frequency of low level clouds. They also found an increase of geometrically thicker clouds over open water. Li et al. (2020b) explained that newly re-frozen sea ice areas can mitigate the development of low level clouds due to the imbalanced heat and moisture sources. Furthermore, the thermodynamic phase distribution of wintertime MPC can be perturbed by sea ice concentration changes due to the convective heat transfer over leads or polynyas (Andreas and Cash, 1999). Papakonstantinou-Presvelou et al. (2022) found that Arctic low-level clouds contain more ice crystals over sea ice than over open ocean, which is attributed to the amount and type of aerosols characteristic of each surface. While sea ice leads have been identified as main wintertime source of sea spray aerosols, there are limitations regarding the quantification of amounts and drivers of sea spray emitted from leads (Lapere et al., 2024).

Using synergistic atmospheric observations ~~onboard~~ on-board the research vessel (RV) Polarstern during the year-long Multidisciplinary drifting Observatory for the Study of Arctic Climate MOSAiC expedition (Shupe et al., 2022) from 2019 to 2020, Saavedra Garfias et al. (2023) have proposed a mechanism to physically link the sea ice states in the vicinity of RV Polarstern with the MPC observed above it. By exploiting a novel high-quality, high-resolution satellite based sea ice lead fraction estimation, which was specifically derived for MOSAiC along the RV Polarstern drifting path (von Albedyll et al., 2024), Saavedra Garfias et al. (2023) found that some properties of MPC when coupled to the sea ice leads via the water vapour transport, are correlated to the upstream sea ice lead fraction. Among those properties the most remarkable is the liquid water path (LWP) which is positively correlated with the amount of sea ice lead fraction. Conversely, the ice water path (IWP) was not found to be correlated with sea ice leads.

The majority of previous studies relating MPC properties and sea ice state either consider large spatial scales or short term observations. This hinders the evaluation of those findings within a climate modelling context. Although models are able to capture several aspects of MPC realistically, they e.g. struggle to accurately represent thermodynamic phase and ice/liquid water path (Schemann and Ebell, 2020; Pithan et al., 2014). At the same time, current climate models do not sufficiently take into account how MPC properties change in a warming climate (Cesana et al., 2025; Nakanishi and Michibata, 2025).

Thus, long-term cloud observations are paramount to evaluate climate models. Manaster et al. (2017) analysed over 20 years of multi-satellite products to estimate global liquid water path (LWP) trends over ~~ocean~~ oceans and evaluated them against CMIP5 models. Although they did not include the polar regions, their results are one of the few references for the long-term rate of change of LWP, with positive trends of about 1-2 $\mathrm{g\,m^{-2}\,dec^{-1}}$ reported for the Southern Ocean and the North Pacific. They also found that discrepancies between observations and CMIP5 models cannot be explained by removing sources of inter-annual variability like El Niño Southern Oscilation (ENSO), concluding that ENSO is not a major parameter to affect the LWP trends. They did however not discard the possibility that other modes of variability could have a larger impact on LWP trends, e.g. the Pacific Decadal Oscillation (PDO).

This brings up two questions: Firstly, can the findings of Saavedra Garfias et al. (2023) obtained for one winter of observations of MPC properties linked to sea ice state in the Central Arctic be confirmed for long-term observations in the Western Arctic? Secondly, are Arctic MPC properties correlated with climate variability modes that are not evident from short-term studies? Answering these questions will advance our knowledge on how ocean-sea ice-atmosphere interaction and feedback processes modulate Arctic cloud properties, which in turn provides valuable information for better representation of MPC in weather and climate models. For this purpose, the present study applies the methodology developed by Saavedra Garfias et al. (2023) to long-term wintertime MPC observations in the Western Arctic ranging from 2011 to 2024 .

The manuscript is organized as follows: in Sec. 2 we present details about the measurement site, instrumentation, data processing, and analysis methods adopted for the present study. Results are presented in Sec. 3. Specifically, the new findings regarding the modulation of MPC properties by sea ice conditions for the entire 14 years as well as the year-to-year-variability and trends are reported in Sec. 3.1 and Sec. 3.2 - Sec. 3.2.3, respectively. These results are further discussed in Sec. 3.3 by highlighting how the present work corroborates or contradicts previous results obtained by the same method from the MOSAiC expedition in the Central Arctic. Finally, Sec. 4 summarizes the implications of our results. Additionally, detailed descriptions of data availability, statistical methods, climatological analysis, nomenclature description, and ancillary results can be found in the appendixes and in the supplementary document, respectively.

2 Data and Methodology

The Atmospheric Radiation Measurement (ARM) program of the US Department of Energy (www.arm.gov) provides long-term comprehensive high-quality observations for clouds and radiation at multiple locations around the world. In particular for Arctic studies one of the few sources of quasi uninterrupted long-term observations is the ARM's North Slope of Alaska (NSA), observational site located at a latitude 71.323° North and longitude of 156.609° West, in Utqiaġvik, Alaska, in the Western Arctic (Fig. 1). In the present study, we utilize cloud observations of fourteen winter seasons ranging from November 1^{st} to April 30^{th} from the NSA site to characterize MPC and investigate the change of their properties governed by different upstream sea ice conditions. For that purpose, the methodology developed by Saavedra Garfias et al. (2023) (hereafter referred to PSG23) is adapted and applied to the suite of instrumentation available at the NSA site, as described in the following section.

Table 1. Specifications of instrumentation, data products and their references used for this study. VAP refers to ARM's Value Added Product.

NSA site observatory					
Instrument/VAP	Full name	Variables/Producs **	Resolution		Reference
			time	range	
MWR RET	passive microwave radiometer	LWP, IWV	1 s	-	Zhang (2024)
MWR LOS*	passive microwave radiometer	LWP, IWV	1 s	-	Cadeddu et al. (2024)
KAZR ARSCL	Ka-band cloud radar	Ze, V_D, S_w, LDR	3 s	30 m	Johnson et al. (2024)
KAZR CORRGE*	Ka-band cloud radar	Ze, V_D, S_w, LDR	3 s	30 m	Toto and Giangrande (2024)
CEIL10m	Ceilometer 10m	β, CBH	16 s	10 m	Zhang et al. (2024)
INTERPSONDE	Interpolated Radiosonde	T, P, $\mathrm{q_v}$, $\boldsymbol{V}$	1 min	20 m	Jensen et al. (2024)
FLUXRAD	Down/upwelling longwave radiation	T_{skin}, Ri_b, PBLH	1 min	-	Riihimaki et al. (2024)
GND_IRT*	Ground Infrared Thermometer	T_{skin}, Ri_b, PBLH	1 min	-	Shi et al. (2024)
Space-borne sensor					
AMSR2	region Chukchi-Beaufort	n3125 SIC	1 day	3.2 km	Melsheimer and Spreen (2019)
AMSR2*	region North West Passage	n3125 SIC	1 day	3.2 km	Melsheimer and Spreen (2019)
SSMIS17*	region North West Passage	n3125 SIC	1 day	3.2 km	Melsheimer and Spreen (2019)
Ancillary data					
ECMWF	Cloudnet Numerical Prediction	all	1 hour	–	O'Connor (2025)
–	Arctic Oscillation index	AO	1 day	-	NOAA AO
–	El Niño Southern Oscillation	ENSO	1 week	-	JPL ENSO
–	Pacific Decadal Oscillation	PDO	1 week	-	JPL PDO

* used as alternative to reduce data gaps. **See appendix E for full definition of acronyms.

2.1 ARM atmospheric remote sensing instrumentation

The primary set of remote sensing instruments from which data was used to characterize MPC are the ARM Ka-band zenith-pointing cloud radar (KAZR), the Vaisala CL31 cloud lidar (ceilometer) and a dual-frequency microwave radiometer (MWR). Moreover, the atmospheric boundary layer parameters and thermodynamic states are estimated from the synergy of ground infrared radiometer (GND_IRT) and radiosondes launched regularly from the NSA site. Table 1 summarizes the instruments, relevant data products, their spatial and temporal resolutions, and a list of corresponding references that are utilized in the present study. A detailed availability time-line for the total period of study is shown in Fig. S14 of supplementary material S4. Additionally, observations of sea ice conditions from space-borne sensors are needed to complement the set of required data for the application of the PSG23 method. The processing and merging of sea ice data with the atmospheric observations is explained in Sec. 2.3.

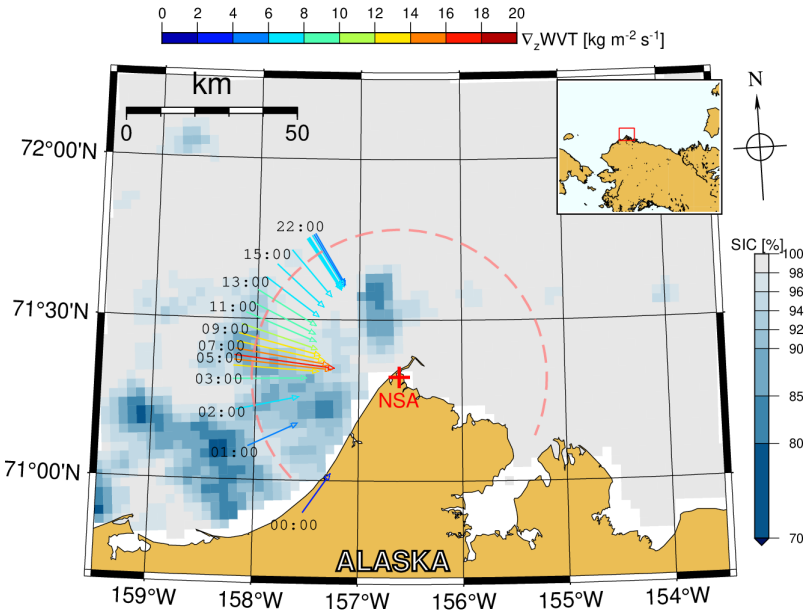


Figure 1. ARM's North Slope of Alaska NSA site (red cross: 71.23° North, 156.61° West) in Utqiaġvik, Alaska (top right inlet). Right-bottom colour scale indicates the AMSR2 sea ice concentration (SIC) from January 19th, 2019. Red-dashed 50 km semi-circle marks the sub-sector around NSA site considered in this study. The coloured radial arrows depict ~~several directions~~ the direction of ∇_zWVT at selected times throughout the day for visualization purposes (see Sec. 2.4) as observed above NSA site.

2.2 Characterization of the cloudy atmosphere

Figure 2 shows an example for the synergy of observations by the KAZR cloud radar, the ceilometer and the MWR for the case of January 19th, 2019. These sets of observations together with the atmospheric thermodynamic information obtained either from the ECMWF numerical weather model (O'Connor, 2025) or radiosonde profiles are the basis for the algorithm that classifies the thermodynamic phase and hydrometeor type of the cloudy atmosphere. The retrieval algorithm utilized in this study is the state-of-the-art Cloudnet target classification algorithm (Illingworth et al., 2007; Tukiainen et al., 2020) version CloudnetPy 1.68.1 shown in Fig. 2 (d). By default the ARM data are not supported by CloudnetPy, therefore the data from the instrumentation listed in Table 1 had to be adapted to be a compliant input (Saavedra Garfias and Kalesse-Los, 2022). In addition to the standard Cloudnet classification products, other atmospheric and cloud properties are calculated, namely: atmospheric boundary layer height, cloud base and top heights, and cloud top temperature for each cloud layer. Readers are referred to PSG23 for details.

Accurate characterization of Arctic low-level stratus clouds is compromised when the base of a liquid-containing cloud layer is detected by the lidar at altitudes below the radar lowest detection range~~: in that case, if the liquid layer extends above~~. As explained in Griesche et al. (2020), the distribution of the LWP depends on whether a higher liquid-containing cloud layer was observed or not. When the low-level stratus cloud attenuates the lidar signal below the radar lowest detection range ~~Cloudnet~~

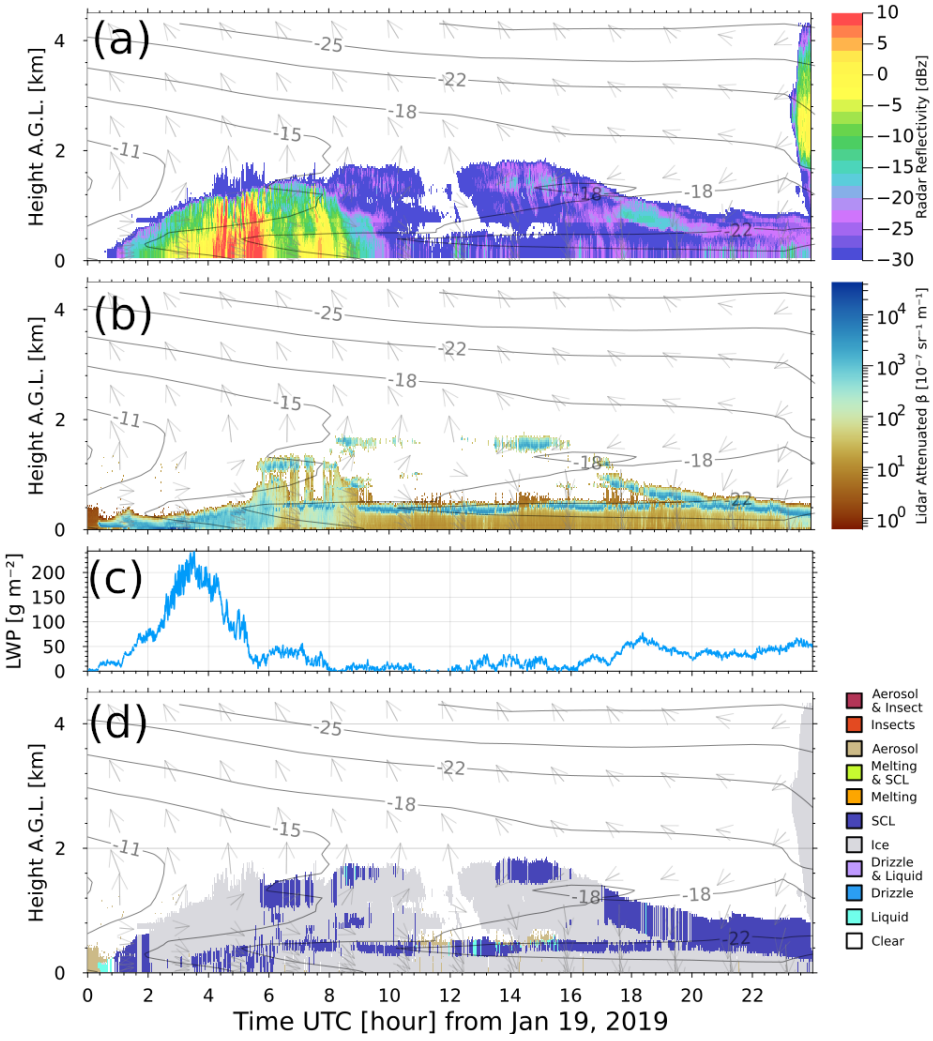


Figure 2. Synergistic ground-based remote sensing observations at NSA on January 19, 2019. Ka-band cloud radar (KAZR) reflectivity factor (a), ceilometer Vaisala CL31 attenuated backscattering coefficient β (b), dual-frequency MWR liquid water path (c), Cloudnet target classification (d) with supercooled liquid (SCL) in blue. Panels (a), (b) and (d) include profiles of the ECMWF numerical weather prediction model horizontal wind vector (arrows) and temperature (iso-therms).

~~misinterprets that cloud as missing liquid layer and classifies as pure ice.~~ no liquid layer is identified by Cloudnet at all and the entire profile is classified as ice. In that case, the LWP from the microwave radiometer is simply ignored (as in Fig. 2 2-3:30 UTC). If an other liquid cloud layer is present higher up, Cloudnet distributes the LWP measured by the microwave radiometer to that layer~~, otherwise Cloudnet ignores the LWP~~. Griesche et al. (2020, 2024) reported ~~for the MOSAiC expedition~~ that such low-level stratus cloud cases occur more than 25% of the observation time. Also, they found for the MOSAiC expedition that low-level stratus are more frequently observed during summer than winter. For the NSA site the lidar can detect liquid

at altitudes as low as 10 m whereas the radar has a lowest detection range of 160/100 m for the KAZR's ARSCL/CORRGE products, respectively (detail in references Table 1). The present study has found that low-level clouds below radar detection range of 160 m (100 m) comprises about 26% (22.5%) of data. To overcome this limitation, in the present study the database is adjusted by a flat extrapolation of KAZR's radar reflectivity ~~is~~ applied down to the lidar liquid layer detection, before the cloud characterization is performed.

Furthermore, one of the main short-comings of the Cloudnet target classification is that cloud liquid detection is solely based on a valid lidar signal. In Fig. 2, at 2-4 UTC, the lidar signal is fully attenuated by liquid within the lowest range gates of the ceilometer. Thus, higher supercooled liquid-layers remain undetected and all pixels without valid lidar signal are classified by Cloudnet as ice. More sophisticated cloud radar Doppler spectra-based tools such as introduced in Kalesse-Los et al. (2022) and Schimmel et al. (2022) would be able to detect liquid beyond full lidar signal attenuation. However, their application would require novel training on the NSA dataset and extensive computing processing time which is beyond the scope of this study. As a takeaway, the amount of MPC detected by Cloudnet used here has a low bias whereas ice-only clouds are overestimated.

The Cloudnet processing chain, applied to 14 years of NSA data, is the backbone for creation of a combined dataset of macro- and micro-physical cloud properties merged with sea ice conditions (as explained in Sec. 2.3) similarly to Saavedra Garfias and Kalesse-Los (2023) ~~.~~ where MPC are considered when LWP and IWP, in a single cloud layer, are equal or greater than 5 $\mathrm{g\,m^{-2}}$ to avoid introducing uncertainties from retrieval algorithms due to instrument minimum detectable capabilities.

2.3 Characterization of sea ice conditions around NSA site

The PSG23 method utilized sea ice lead fraction (LF) at a high spatial resolution of 700 m. LF was derived from sea ice divergence imaging from Synthetic Aperture Radar satellite specifically developed for the MOSAiC expedition (von Albedyll et al., 2024). That quality level of LF product does not exist for the multi-year observations at the NSA site, which is a major difference for the application of the PSG23 method in the present study. Instead, sea ice concentration (SIC) is obtained from the University of Bremen public repository (www.seaice.uni-bremen.de, e.g. (Spreen et al., 2008; Melsheimer and Spreen, 2019)) to characterize the ocean conditions surrounding NSA site. SIC is retrieved from brightness temperatures observations by the Advanced Microwave Scanning Radiometer-2 (AMSR2) sensor which has been in operation onboard the Global Change Observation Mission 1st GCOM-W1 satellite since autumn 2012. The product retrieved is the AMSR2 sea ice (ASI) concentration at a Polar stereographic grid size of 3.124 km and daily temporal resolution (Spreen et al., 2008) (see "Space-borne sensor" in Table 1). The University of Bremen provides ASI products for the whole Arctic as well as selected regions of interest. The present study uses the regions identified as "Chukchi-Beaufort" (Fig. 1) which is centered close to the NSA site longitude and covers the western- and eastern-part of the Chukchi and Beaufort seas, respectively. Furthermore, from the whole "Chukchi-Beaufort" sector only a small subset of grid cells are considered to be relevant for the PSG23 method, i.e. sea ice conditions that are most likely to interact with the atmospheric boundary layer clouds at the NSA site (Sec. 2.2). The sub-sector considered for the present study is a semi-circle centered at NSA site with 50 km radius and limited from -125° to 110° azimuth (red-dashed delimited semi-circle sector in Fig.1). Because we are exclusively interested in the sea ice-cloud interaction, the

complementary semi-circular sector covering the land is dismissed. This means MPC with CTH $\leq$ 3 km being advected from the land to the NSA site are excluded from this study, which corresponds to $\sim$8.1% of the data.

Mean and standard deviation of the SIC are used here. It is assumed that SIC follows a truncated normal distribution with lower and upper truncation limits of 0% and 100%, respectively. The PSG23 method considers only a conical sector extending from the NSA site outwards up to 50 km with angular width of $\pm 3°$. The azimuth of the conical sector is governed by the horizontal wind vector $\boldsymbol{v}_w$ at a height where $\nabla_z \mathtt{WVT}$ is at maximum (details in Sec. 2.4). Subsequently, the mean sea ice concentration within the conical sector is denoted by SIC, whereas the mean sea ice concentration for the entire 50 km semi-circular sector (red-dashed in Fig. 1) is denoted by $\mathrm{SIC}_{\odot}$ (Fig. 3). Details about the yearly difference between the statistics given by the entire circle around NSA site $\mathrm{SIC}_{\odot}$ and the conical sector SIC aligned to $\boldsymbol{v}_w$, are shown in Fig. S1 in supplement S1.1.

Between 2011 and 2024, the Chuckchi-Beafort seas area experienced winters with extraordinary low sea ice concentration ($\mathrm{SIC}_{\odot} \lesssim$50% in Fig. 3 and Fig. S1), e.g. 2012/13, 2016/17, 2017/18, 2019/20, 2023/24, and 2024/25. These anomalously low sea ice winters can be partially related to climatological variability and/or forcing from low latitudes. For example, using observations and model simulations for the Barents-Kara seas area Zhang et al. (2023) revealed that the decrease of sea ice area is correlated with an increase of the frequency of atmospheric rivers reaching the Arctic in winter. They prevent the sea ice recovering from summer melt and from growing to the climatologically expected sea ice coverage in winter. For the Chukchi-Beaufort seas, and for the period 2011 to 2020, the frequency of atmospheric rivers (averaged over November to April) has maximum values of 5.3% in 2018/19, an intermediate value of 2.6% in 2013/14, 2014/15, and 2019/20, plus a minimum value of 0.2% in 2015/16 (personal communication with Zhang et al. (2023) lead author). The wintertime 2018-2019 with a less frequent but still noticeable $\mathrm{SIC}_{\odot} \lesssim$50% in Fig. S1, can be attributed to the anomalous warm ocean water as response to the southerly winds associated with episodic atmospheric blocking over the Bering Sea in September 2018 which was directly observed by the R/V Mirai Arctic Expedition in November 2018 (Kodaira et al., 2020).

2.4 Coupling sea ice - atmosphere via water vapour transport

Winter sea ice open areas (e.g. leads or polynyas) are effective local sources of heat and moisture released to the atmosphere. Because of convection and advection, plumes of heat and moisture can be transported afar from the location where the sea ice lead or polynya occurs and interact with the clouds. This interaction is needed to be established in order to relate the sea ice concentration and the cloud properties. This is performed by applying the PSG23 methodology. Whether a cloud is influenced by the sea ice-ocean system or not is determined by taking advantage of the water vapour transport (WVT) as a physical mechanism to link the upstream sea ice conditions and the measured cloud properties above the NSA site. Specifically, the WVT, which is estimated from radiosonde profiles, was proposed by Saavedra Garfias et al. (2023) to physically link, akin a conveyor belt, the heat and moisture released by sea ice openings and transport them downstream to interact with the cloud ~~(~~over an observatory location ~~)~~ and perturb its properties.

The WVT normally consists of several bands of different magnitudes along the vertical profile. In order to determine which bands are the most relevant to be interacting with a cloud, the PSG23 method limits the WVT vertical profile to the planetary

boundary layer height (PBLH), which is estimated by the bulk Richardson number when it is $Ri_b \approx 1$. The PSG23 method determines the most relevant WVT band (if several are present) by means of its vertical gradient ($\nabla_z \mathtt{WVT}$ [$\mathrm{kg\,m^{-2}\,s^{-1}}$]) calculated using Eq. 1. Please note that a detailed derivation is given in Saavedra Garfias et al. (2023). In summary, to classify cases where the WVT is coupled or decoupled to the cloud, the cumulative variance of virtual potential temperature θ_v is analysed from the cloud base/top height downwards/upwards to bottom/top altitudes where the variance exceeds a certain threshold. These altitudes are then assigned as cloud mixing layer limits. When the $\nabla_z \mathtt{WVT}$ vertical profile has a local maximum at an altitude within the cloud mixing layer limits, that cloud is assigned to be coupled (denoted as "co") to the sea ice-WVT system, otherwise is considered to be decoupled (denoted as "de"). $\nabla_z \mathtt{WVT}$ is calculated as

$$\nabla_z \mathtt{WVT} = -\frac{10^2}{g} \left| q_v \cdot \boldsymbol{v}_w \right| \frac{dP}{dz} \tag{1}$$

where ∇_z indicates the vertical gradient, g is the constant of gravity, with the specific humidity q_v [$\mathrm{g\,kg^{-1}}$], horizontal wind speed $\boldsymbol{v}_w$ [$\mathrm{m\,s^{-1}}$], and air pressure P [Pa] at altitudes z [m].

From all ASI grid cells within the 50 km semi-circle centered at NSA site, only SIC cells are considered that are located within the conical sector of $\pm 3°$around the upwind direction. An example is shown in Fig. 1 where the radial arrows depict the direction of $\nabla_z \mathtt{WVT}$. Arrows are color-coded by the maximum $\nabla_z \mathtt{WVT}$. At a given time the azimuth of the conical sector is governed by the upwind direction obtained from the altitude where reaches its maximum. In the following, the statistics are based uniquely on sea ice concentration present within the $\pm 3°$conical sector. Situations with winds coming from the land (i.e. Southerly flow) are not considered in the analyzed dataset. Figure S1 stresses the fact that the sea ice conditions around NSA site are of completely different statistically nature than the sea ice conditions within the $\pm 3°$conical sector that interacts with the clouds above NSA site. Therefore, relating cloud characteristics observed from satellite or in-situ observations with a large area of sea ice can lead to ill-posed correlations since not all sea ice conditions play a relevant role to explain observed cloud properties (e.g. Palm et al. (2010); Li et al. (2020a, b)).

2.5 NSA site atmospheric pressure systems and climatology

~~Atmospheric~~ The NSA site climatology is characterized by the persistent influence of cyclonic activity in the north-western Pacific Ocean and anticyclones in the Beaufort/Chukchi seas (Serreze et al., 1993; Serreze and Barry, 2014). Thus the atmospheric surface pressure is a useful indicator of events characterized by synoptically high (H-) or low (L-) pressure systems over NSA site (Fig. 3). Atmospheric air temperature and pressure are closely related to stability or instability in the atmosphere which strongly influences the formation of clouds. The classification of local pressure system at any given time and base on measured local pressure and temperature is estimated by the following steps: i) a reference virtual isobaric surface P_0 is assumed to separate the H- or L-pressure observations, ii) from the measured surface pressure and temperature, the relative height of the virtual isobar P_0 is determined. The relative height of P_0 is expressed in terms of geopotential height difference derived

from the equation of state (Rogers and Yau, 1991):

$$\Delta Z = \frac{R\overline{T}}{g_0} \log\left(\frac{P_0}{P}\right) \tag{2}$$

where R is the specific gas constant 287.05 $\mathrm{J\,kg^{-1}\,K^{-1}}$, g_0 the acceleration of gravity at the surface 9.81 $\mathrm{m\,s^{-2}}$, $\overline{T}$ the mean temperature within the layer [K], P_0 the reference isobar surface (in this case the mean sea level pressure of 101.32 kPa), and P is the measured local surface pressure [kPa] at a given time. ΔZ takes negative values for observations with a H-pressure (i.e. P>P_0), conversely ΔZ is positive for L-pressure (i.e. P<P_0). The $\overline{T}$ is assumed to be the measured 2 m air temperature, and its effect is to adjust the magnitude of ΔZ when P considerable departures from the reference P_0. Within the analysed winters from 2011 to 2024 , surface pressures measured at NSA are biased towards H-pressure with a median of 101.69 kPa and Inter-Quantile Region (IQR) of 100.95 to 102.50 kPa. H-pressure systems were observed slightly more frequently (56.3% of the time) than L-pressure systems (43.7% of the time). The distribution of ΔZ reveals an ample difference when sorted by the corresponding cloud observations' coupled or decoupled classification. ΔZ for coupled cases have a median of -9.45 m (IQR: -65.05 m, 44.72 m). In contrast decoupled cases have a median of -30.98 m (IQR: -86.95 m, 18.74 m). Accordingly, H-pressure systems favour the formation of decoupled clouds. It is important to note that ΔZ is meant to be a representation of the local pressure at NSA site and cannot be taken as a substitute to synoptic pressure systems for the Western Arctic found in weather maps.

3 Results and discussion

NSA site wintertime (November 1^{st} to April 30^{th}) observations from 2011 to 2024 were analysed in accordance with the methodology outlined in the previous sections. The results are presented after the observations ~~were~~ from the instruments listed in Table 1 were resampled to a common 1 minute time resolution and clustered between high (ΔZ<0) and low (($\Delta Z \geq$0)) pressure weather systems and coupled (co), decoupled (de) status. Statistics of wintertime cloud properties are reported based on two approaches: as a function of SIC as in Saavedra Garfias et al. (2023) (Sec. 3.1), and as time series along the 14 years (Sec. 3.2). The results are presented as descriptive statistics by the ~~distribution's~~ distributions median ($\mu_{½}$) and ~~distribution's~~ distributions variability by the median absolute deviation (MAD) defined by $\sigma_{\text{mad}} = \pm median(|X_i - \mu_{½}|)$. Other statistical distribution descriptors have been used, for example the geometric mean (μ_g), the 25^{th}, and 75^{th} percentiles, however, if not explicitly noted otherwise, the following results are referring to $\mu_{½} \pm \sigma_{\text{mad}}$.

3.1 Modulation of MPC properties as a function of SIC, coupling status, and pressure system

For the considered time period the cloud frequency of occurrence (FoO) were analysed. The total cloud FoO (Fig. 4, left bars) shows a roughly constant FoO at about 75% throughout the wintertime, with a dependency on SIC for the distribution of cloud FoO during the different winter months. For MPC (Fig. 4, right bars) the FoO shows a reduction from start to end of winter from about 56% in November to about 40% in April, with the largest contribution from SIC>95% happening in January. The total cloud FoO (left bars) were derived from all observations of clouds with CTH $\leq$ 3 km and MWR-LWP > 0 $\mathrm{g\,m^{-2}}$ or

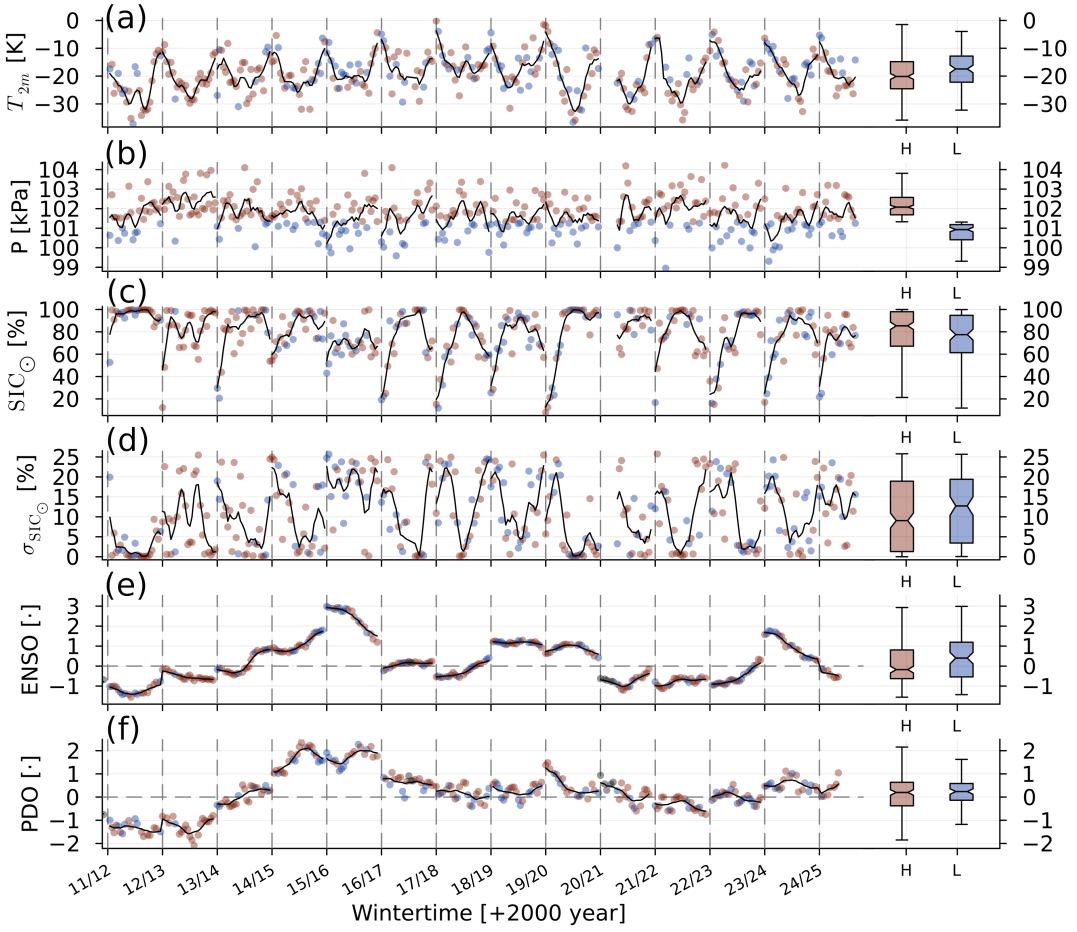


Figure 3. Wintertime climatology for the NSA site as time series from 2011 to 2024 for: (a) 2 m air temperature, (b) surface atmospheric pressure, (c) average $\mathrm{SIC}_\odot$ within the whole 50 km semi-circle around NSA site, (d) standard deviation of $\mathrm{SIC}_\odot$, (e) ENSO index, (f) PDO index. ~~Circle symbols indicate~~ For visualization purposes the data is shown as weekly averages (circles), the solid black line is the weekly moving average. The vertical dashed lines indicate the jump from end of April to November, thus the apparent discontinuity at these lines is not physical. On the right of each panel the whole data distribution is shown as boxplot separated according to Eq. 2 for H- and L-pressure systems in light-red and light-blue, respectively.

IWP > 0 $\mathrm{g\,m^{-2}}$ referring to cloud liquid and cloud ice detections. The MPC occurrence is from where both the MWR and radar have detected liquid and ice simultaneously. The fact that for every month there are occurrences of SIC=0%, indicates the constant presence of polynyas and leads during wintertime along the SIC semi-cone around the NSA site. It is important to note that the SIC shown in Fig. 4 is the average within the semi-cone (50 km radius and 6° wide) with the azimuth being determined by the WVT direction.

The absolute values for total cloud and MPC are in line with other studies such as Shupe et al. (2011) reporting an annual total cloud FoO of around 80% at NSA and Shupe et al. (2006) reporting a MPC FoO of around 40% at NSA in fall.

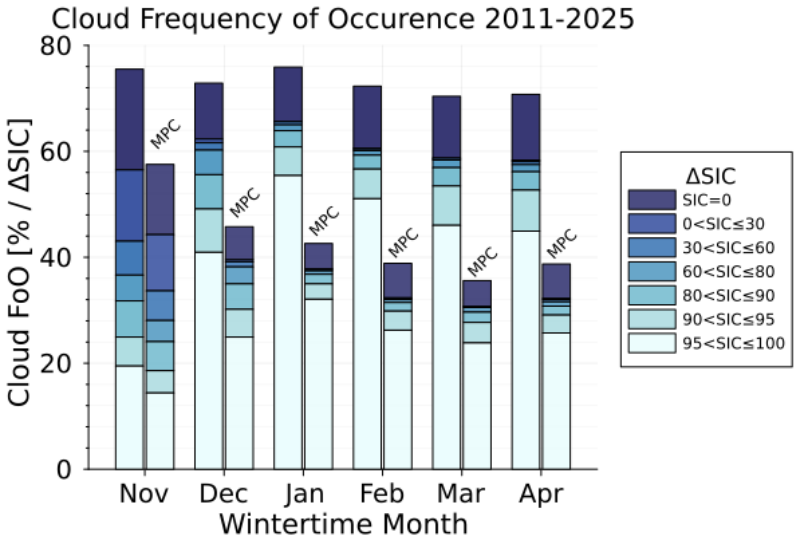


Figure 4. FoO for total (left bars) and mixed-phase clouds (right bars) per month for wintertime from 2011 to 2025. The FoO is based on cloud events in a month versus total days in a month.

To investigate the ~~effects~~ relationship of sea ice ~~on the~~ with cloud properties, the data are sorted as a function of SIC with a bin width ~~centered~~ centred every 20^{th} percentile. The MPC property is represented by the median $\mu_{1/2}$ and its MAD σ_{mad} of its distribution contained within a specific SIC bin. Note that for the following analysis the MPC detection were constrained to cases with LWP and IWP above 5 $\mathrm{g\,m^{-2}}$ to reduce noise due to the minimum detectable in the retrievals, similar as in PSG23 method.

Figure 5 presents the liquid water path (LWP), cloud droplet effective radius r_{eff}, ice water path (IWP), and ice particle effective radius r_{eff} as a function of the upwind sea ice concentration along the $\pm 3°$ of the maximum $\nabla_z \mathtt{WVT}$ direction. Observations from H-pressure systems are shown on the left side (Fig. 5 a,c,e,g) and L-pressure on the right side (Fig. 5 b,d,f,i). The upwind $\nabla_z \mathtt{WVT}$ coupled/decoupled cases are indicated by blue-circles/orange-triangles, respectively. For clarity, circles and triangles belonging to the same SIC bin are displaced by -3%. To describe the data behaviour, the empirical model's best fit is indicated by the solid ~~colored~~ coloured lines, the 95% confidence interval (CI) is marked as shadowed area around the solid lines along with the coefficient of determination r^2 and goodness of fit χ^2 for coupled (blue) and decoupled (orange) cases as defined in App. A, Eq. A3 and Eq. A2, respectively.

The results in Fig. 5 reveal the tendency for several microphysical cloud properties to increase in magnitude as SIC decreases. ~~The lower SIC gets, the less pronounced the increase in cloud microphysical property becomes until it reaches a certain plateau where the property levels off.~~ It has been found that the best empirical model representing the described behaviour is given by Eq. 3 with a ~~level-off value of~~ maximum trending to $\beta_1 + \beta_2$ for SIC$\rightarrow$0%. This empirical model has been chosen specifically

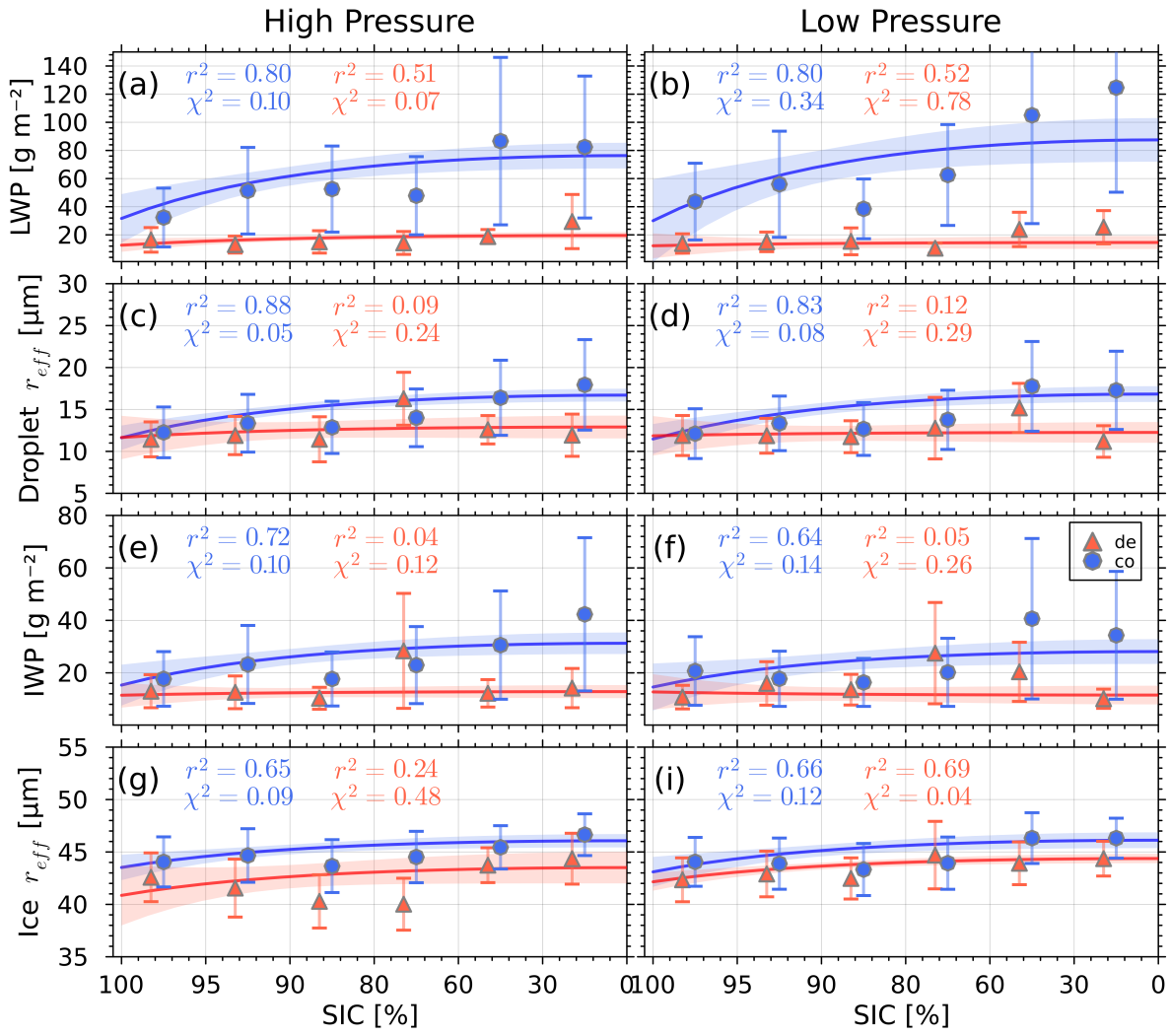


Figure 5. Cloud microphysical properties as a function of SIC (for SIC>5%) for coupled (blue circles) and decoupled (orange triangles) classes during the wintertime period from 2012 to 2024. H-/L-pressure systems are arranged on the left/right columns, respectively. Liquid water path (a, b); droplet effective radius (c,d); ice water path (e,f); ice effective radius (g,i). Symbols/bars represent the median/$\pm\sigma_{\text{mad}}$ for the distribution within SIC bins of every 20^{th} percentile. Lines indicate the best fit with 95% confidence interval (CI) shading around the solid lines. The r^2 and χ^2 are the best fit indicators for the model Eq. 3 for coupled/decoupled. Note that x-axis ticks and labels are not equidistant.

to best fit the coupled cases, thus when the fit is not the best for decoupled cases it is an indicator for the difference between coupled/decoupled cases. For decoupled cases, only few cloud properties have a clear relation with SIC. For many variables

no correlation was found.

$$\mathcal{F}_{var}(\text{sic};\boldsymbol{\beta}) = \beta_1 + \beta_2 \exp\left(\text{sic}^2\right) \tag{3}$$

where sic $\in \{0,\ldots,1\}$ is the normalized sea ice concentration, $\mathcal{F}_{var}$ is the observed cloud property to be examined as a function of sic (for instance LWP, IWP, droplet r_{eff}, ice particle r_{eff}). β_1, β_2 are the empirical coefficients obtained from the best non-linear curve fit. In this study Eq. 3 was favoured over the power law function proposed as $\mathcal{F} = aSIC^b$ by PSG23. The reasoning for that is that during MOSAiC wintertime the observed SIC were mostly above 90% (with sparse cases of SIC between 80% and 90%). Contrarily, the present study covers SIC observations ranging from 0% to 100% during the 14 years providing a more complete picture for the sensitivity of cloud properties to change as a function of SIC.

Specifically in Fig. 5, panels (a) and (b) reveal a clear relationship between LWP and SIC in coupled cases: LWP (blue circles) increases as sea ice coverage diminishes. Specifically, LWP increases steadily until it levels-off at a median value of $\sim$80 to 120 $\mathrm{g\,m^{-2}}$ for SIC$\lesssim$30%. Moreover, when the observations are sorted according to the presence of H- or L-pressure weather systems at NSA site, further differences are found. For instance, the data fits Eq. 3 better for the H-pressure (r^2=0.80 and χ^2=0.1), than for the L-pressure cases (r^2=0.80 but χ^2=0.34). In addition, for L-pressure, LWP data is more variable which results in larger uncertainties for the β_1 and β_2 parameters in Eq. 3 (i.e. wider shaded area around best fit line in Fig. 5 (b)), especially due to outliers that can be spotted at around 90-80% SIC. The found behaviour of LWP for decoupled cases (orange triangles), is in agreement with findings by Saavedra Garfias et al. (2023) confirming that LWP in decoupled scenarios does not follow any significant relationship with SIC. This is supported by largely reduced r^2 of 0.51/0.52 for H-/L-pressure cases, respectively. Droplet effective radius r_{eff} (Fig. 5 (c) and (d)) shows similar behaviour as LWP, with the coupled droplet r_{eff} being strongly negatively correlated with SIC. At the same time, droplet r_{eff} was not found to be correlated with SIC for decoupled MPC clouds.

Regarding IWP, Fig. 5 (e) and (f) contrast the MOSAiC findings that IWP does not exhibit any change in relation with different SIC values. Instead, at NSA site a ~~positive correlation with~~ high correlation between increasing IWP in decreasing SIC situations was found for coupled cases with r^2 as high as 0.72 for H-pressure cases. For decoupled cases however, IWP does not present any statistically significant difference as SIC changes. Within a pan-Arctic perspective and from satellite observations Cesana et al. (2024) found out that for winter time the cloud cover classified as ice increases as SIC decreases (negative correlation), and cloud cover classified as mixed-phase are even strongly negative correlation with SIC, which is in agreement with our results, albeit the temporal and spacial scales of both studies are different.

In coupled scenarios, the ice effective radius (Ice r_{eff}, Fig. 5 (g) and (i)) shows a significant relationship with SIC when fitted to Eq.3 as it is indicated by their r^2=0.65/0.66 and χ^2=0.09/0.12 (Fig. 5 (g) and (h) for H-pressure and L-pressure cases), respectively. However, the change in magnitude of ice particle r_{eff} for changing SIC is less pronounced compared to cloud droplet r_{eff}. Interestingly, for ice r_{eff} in decoupled situations, a similar relationship is observed albeit with more widely scattered data that reduces the r^2 to 0.24 for H-pressure cases. Moreover, decoupled LWP, IWP, droplet r_{eff}, and ice r_{eff} have systematically lower values as their counterparts in coupled situations.

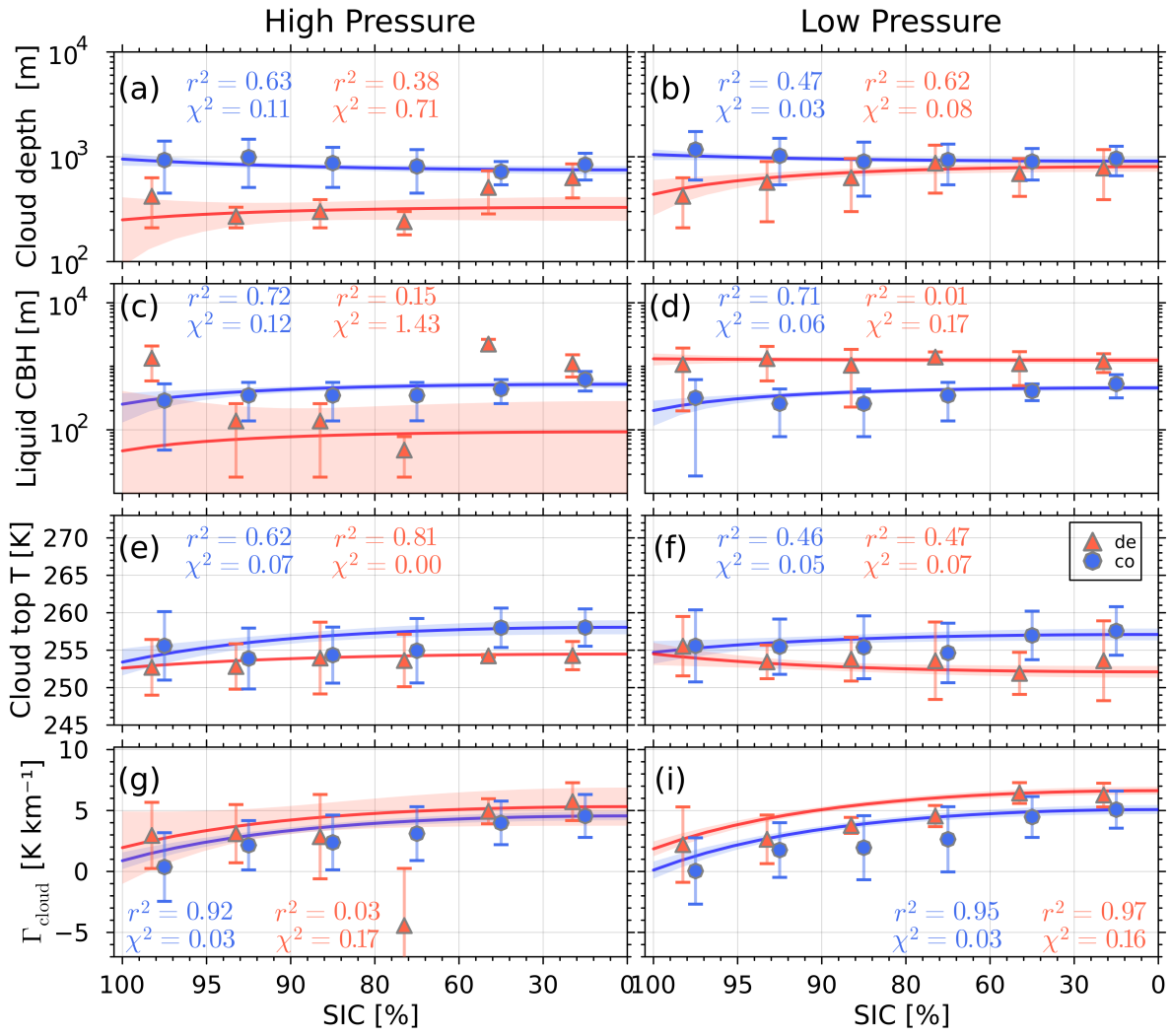


Figure 6. Same as Figure 5 but for cloud depth (a, b); liquid layer cloud base height (c,d); cloud top temperature (e,f); cloud layer temperature lapse-rate (g,i). Symbols (bars) represent the distribution's median (±MAD) for SIC bin widths at every 20^{th} percentile.

A set of MPC macrophysical properties are displayed in Fig. 6: Cloud geometrical depth (δ_h: cloud top minus cloud base heights) in Fig. 6 (a) and (b), liquid layer cloud base height (CBH) in Fig. 6 (c) and (d), cloud top temperature (CTT) in Fig. 6 (e) and (f), and cloud layer temperature lapse-rate (Γ_{cloud}) in Fig. 6 (g) and (i).

Fig 6 reveals that mostly decoupled MPC macrophysical properties and SIC have no clear correlation. This is e.g. evident from the coefficient of determination r^2 of 0.38 for δ_h and of 0.15 for CBH especially for MPC observed in H-pressure system situations, respectively. For coupled MPC cases a clear relationship of δ_h and SIC is found, with cloud depth tending to decrease as SIC decreases (r^2=0.63). With reference to the results from the MOSAiC expedition, the findings that can be confirmed are:

for coupled cases δ_h/CBH are thicker/lower than their decoupled counterparts, independent of SIC with the exception of higher liquid CBH in coupled cases when H-pressure are present.

The results for CTT (Fig. 6 (e) and (f)) show some statistically significant difference between coupled/decoupled cases. Nonetheless, a noticeable dependency to SIC can be identified, with colder CTT for sea ice covered ocean and warmer CTT for large areas of open water ~~, with the only exception for decoupled clouds and H-pressure~~ (see Fig. 6 (e, f)). The model Eq.3 fits better in decoupled cases (r^2=0.81 and ~~r^2=0.47 for H- and L-pressure, respectively~~H-pressure) as compared to coupled cases (r^2=0.62~~and r^2=0.46), respectively~~). For coupled cases, CTT is generally slightly higher than for decoupled cases.

The temperature lapse-rate within a cloud layer is defined as ~~$\Gamma_{\text{cloud}} = -\left(\frac{T_{\text{top}} - T_{\text{base}}}{CTH - CBH}\right)$~~ $\Gamma_{\text{cloud}} = -\sum_{z=\text{CBH}}^{\text{CTH}} \left(\frac{T_{z+1} - T_z}{H_{z+1} - H_z}\right)$, is the single macrophysical property that poses a pronounced modulation of its magnitude as a function of SIC (Fig. 6 (g) and (i)). The Γ_{cloud} under H- and L-pressure systems depicts a systematic bias with Γ_{cloud} for decoupled cases having larger values than the coupled cases~~, mainly for SIC$\gtrsim$60%.~~ . Moreover, Γ_{cloud} observations are well represented by the empirical model Eq. 3 with a robust coefficient of determination of r^2=0.95 and χ^2=0.03 for the L-pressure and coupled cases. The dynamic of Γ_{cloud} ascribed by SIC suggests that for conditions with dominant sea ice coverage (SIC$\gtrsim$95% for H-pressure and L-pressure systems) the coupled lapse-rate median (blue dots in Fig. 6 (g) and (i) SIC>95%) shows that about the half of the Γ_{cloud} distribution is found to be negative. This implies a temperature inversion within the cloud layer ($T_{\text{top}} > T_{\text{base}}$). When SIC decreases e.g. SIC<95%, Γ_{cloud} becomes clearly positive (i.e. $T_{\text{top}} < T_{\text{base}}$) meaning the cloud temperature cools with height, resembling a moist adiabatic process.

The behaviour of micro- and macro-physical properties as a function of SIC suggest that as SIC decreases shallower clouds are observed (Fig. 6 (a,b)), at the same time higher LWP and IWP are found as SIC decreases (Fig. 5 (a,b,e,f)). That apparent contradiction is realized by the increase of liquid- and ice r_{eff} with the decrease of SIC (Fig. 5 (c,d,g,i)). Furthermore, it was found that the lower atmosphere temperature (T2m) positively correlates some of the MPC's micro- and macro-properties, mainly for coupled cases. The physical explanation for the observed increase in LWP and IWP with the decrease of SIC (i.e. warmer surface) is given by the fact that SIC decrease (T2m increase) indicates that more latent and sensible heat fluxes are released by opening in the seaice to the lower atmosphere, favorable for convection and sea salt release, and when that is coupled to the clouds it drives the increase of the MPC parameters. These findinds are aligned with in-situ measurements in Svalbard suggesting that a warming Arctic favours the increase of highly active ice nucleating particles, thus allowing the formation of ice-containing clouds at warmer temperature (Tobo et al., 2024). Similarly, Schäfer et al. (2025) using Arctic MPC simulations found an increase in cloud ice water content with a warming climate due to the increase of ice-nucleating particles and the rime splintering process and secondary ice production.

3.2 Year-to-year variability and trends

In this section, MPC properties are clustered for each considered winter and then ~~analyzed~~ analysed as time series to study year-to-year variability and/or trends. No separation for SIC variation has been made here. Each data point in the time series is comprised of descriptive statistics from the distribution of observations from a given wintertime referred to using the nomenclature "2012/13" to represent, for example, wintertime (WT) from 1st November, 2012 to 30 April, 2013. The time series

is composed of 14 years denoted as $WT = \{2011/12, 2012/13, \ldots, 2024/25\}$, and the MPC micro- and macro-physical properties are studied as a function of WT.

A first attempt to analyse MPC time series observations at NSA site has been reported by Saavedra Garfias and Kalesse-Los (2024) for only coupled/decoupled classes for a shorter period of 10 years. Firstly, these preliminary findings stressed the oscillatory nature of the magnitude of some MPC properties with time. Secondly, a lack of statistically significant trends which were estimated directly using Ordinary Linear Regression (OLR) from the wintertime average was reported. That trend estimation approach, however, suffers of two major shortcomings: i.e. heteroskedasticity and residuals' bias with skewed distributions. Both make the applicability of OLR questionable. Heteroskedasticity happens due to a distribution's variability being higher when the median values are larger; i.e. the larger the median LWP the wider its variance in a given wintertime. The second shortcoming occurs due to the oscillatory time series, e.g., a local maximum LWP was found at 2016/17 between two local minima in 2013/2014 and 2018/2019 respectively. This results in the regression residuals to be biased with skewed distributions towards large LWP values, i.e. residuals do not adhere to a normal distribution with population mean of zero.

To overcome these shortcomings the oscillatory nature of the signal needs to be considered. This is achieved by exploring two commonly used methods in time series analysis (Chang et al., 2021):

i. the oscillatory magnitude is eliminated by using a moving window average over all time series data points with an running window of 10 years. For example, the data point for 2016/17 is averaged over ± 5 winter seasons. Then a weighted linear regression (WLR) is applied. The WLR is an efficient way for fixing heteroskedasticity in linear regression.

ii. the signal is considered to follow a natural cycle with a frequency occurring within the 14 years period. For example, oscillations alike any Arctic intradecadal climate variability that has the potential to modulate the sea ice or cloud properties. In this case a non-linear regression with cyclical terms (Harmonic functions) needs to be applied.

In both methods the distribution variance of cloud properties within a wintertime period is taken into account by applying a weighted regression, with the weights being proportional to the inverse of the variance as given by Eq. A1 where $\sigma \equiv \sigma_{\text{mad}}$ when the fitting is performed over the median $\mu_{1/2}$ or the standard deviation when the mean is used. The time series WLR fitting model to be applied for the methods ***i*** and ***ii*** are given by:

$$\mathcal{Y}(t;\boldsymbol{\beta}) = \begin{cases} \beta_1 + \beta_2 t + \varepsilon & \text{method } \boldsymbol{i}. \quad (4a) \\ \beta_1 + \beta_2 t + \beta_3 \cos(2\pi\nu_k t - \beta_4) + \varepsilon & \text{method } \boldsymbol{ii}. \quad (4b) \end{cases}$$

where $\mathcal{Y}(t;\boldsymbol{\beta})$ is the time dependent cloud parameter to be fitted (e.g. LWP, IWP, cloud droplet/ice particle r_{eff}, etc.) in accordance with method ***i*** or ***ii***. In Eq. 4, t runs over the sequence of wintertime WT and the coefficient to fit is denoted by the vector $\boldsymbol{\beta} = [\beta_1, \beta_2, \ldots]$, and ε represents the model residuals. In both Eq. 4a and 4b the time series trend is determined from $\frac{\Delta\mathcal{Y}}{\Delta t} \equiv \beta_2$. For Eq. 4b, ν_k is an extra parameter, with units of yr^{-1}, that represents the frequency of the oscillating signal with phase shift β_4. Note that in Eq. 4b, ν_k is not an element of the fitting coefficients vector $\boldsymbol{\beta}$ but rather a so-called "free parameter", i.e. its value is not determined by the regression's best fit from the time series data. Instead it is obtained from an external source; the selection of this free parameter is presented in detail later in Sec. 3.2.2.

In the following, the results from time series analysis is presented according to methods *i* (Sec. 3.2.1) and *ii* (Sec. 3.2.2), followed by a comparison of the results by both methods.

3.2.1 Method *i*: Trend estimation using moving-average time series

Using the time series of MPC properties after smoothing the data by the moving average method, the data is fitted to Eq. 4a by applying WLR. The trend is then assumed to be the fitted parameter β_2 and the results are assorted by the cloud coupling class and pressure system at NSA site.

Figure 7 depicts the time series of selected MPC properties that exhibit the largest variability along the years, namely LWP, liquid CBH and CTT. As in previous figures the MPC properties are separated by coupled (blue circles), decoupled (orange triangles) status and pressure system. A distinctive variability of LWP per wintertime is evident, which is reflected by the magnitude of the trends for coupled LWP of +4.4$\pm$0.7 $\mathrm{g\ m^{-2}\ dec^{-1}}$ for H-pressure and +24.3$\pm$0.7 $\mathrm{g\ m^{-2}\ dec^{-1}}$ for L-pressure in Fig. 7 (a) and (b), respectively. The decoupled LWP confirm the systematically lower values compared to the coupled counterparts (as in Sec. 3.1) in this time series perspective. Decoupled LWP also show more stochastic variability resulting in a less pronounced and negative trend for L-pressure system of -5.3$\pm$0.7 $\mathrm{g\ m^{-2}\ dec^{-1}}$.

The liquid layer CBH time series is shown in Fig. 7 (c) and (d). This property also has a noticeable evolution along the years for H- and L-pressure systems, with the first having similar positive trends (+54.3$\pm$0.7 $\mathrm{m\ dec^{-1}}$) and (+54.9$\pm$1.0 $\mathrm{m\ dec^{-1}}$) for coupled and decoupled CBH, respectively; whereas CBH for L-pressure depicts the opposite trends (coupled: almost no trend with +7.5$\pm$0.7 $\mathrm{m\ dec^{-1}}$, decoupled: -134.5$\pm$0.8 $\mathrm{m\ dec^{-1}}$).

Similar as in Sec. 3.1, Fig. 5 for variable SIC regimes, CTT does not show a distinct magnitude difference for coupled and decoupled cases, the same is found in time series basis (Fig. 7 (e) and (f)). In general, the wintertime CTT median has the tendency to slightly decrease over time, albeit the strength of that reduction depends on the coupled status and pressure system. The largest reduction happens for H-pressure and coupled cases (trend: -1.6$\pm$0.6 $\mathrm{K\ dec^{-1}}$) and the lowest for L-pressure decoupled cases with a non-significant trend of -0.9$\pm$0.8 $\mathrm{K\ dec^{-1}}$.

3.2.2 Method *ii*: Trends estimation considering cyclical time series

Given the oscillatory nature of observed time series of MPC properties, first reported by Saavedra Garfias and Kalesse-Los (2024), in the present study we propose the hypothesis that those oscillations might be induced by the climate variability at intra-decadal time scales. Generally speaking, climate teleconnections can influence the formation or melting of sea ice in the Arctic, as a result of which MPC properties are changed according to the findings from previous Sec. 3.1. That might imply the observed MPC time series fluctuations can be explained by the modulation of relevant climate modes in the Arctic. The motivation to postulate this hypothesis is twofold: Firsty, there are numerous studies supporting climate teleconnections between the Tropical Pacific, sub-tropical regions and the Arctic (Timmermann et al., 2018; Kodaira et al., 2020; Zhang et al., 2023; Deng and Dai, 2024; Zhong et al., 2024). Secondly, a noticeable pattern of MPC time series that resembles the ENSO or PDO evolution along the study period; for instance, Fig. 7 (a) and (b) where LWP time series present a crest closely aligned with strong El Niño events (positive ENSO in 2016 and 2023 in Fig. 3). Conversely LWP time series' minima show parallels

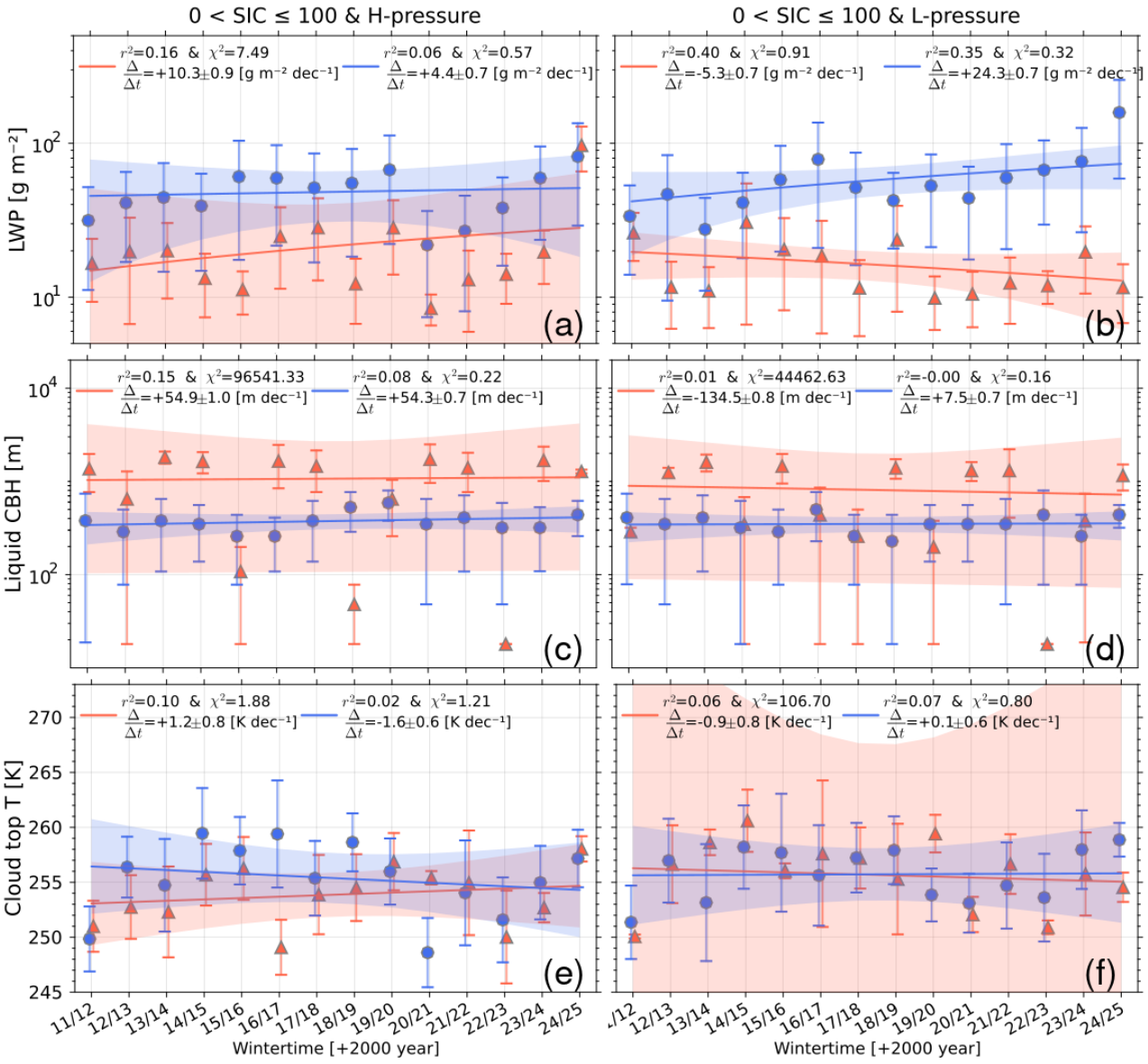


Figure 7. MPC time series for coupled (blue circles) and decoupled (orange triangles) represented by the median ($\mu_{1/2}$) and σ_{mad} (bars) of wintertime distributions. H-pressure (left column) and L-pressure (right column) for LWP (a, b), liquid layer CBH (c, d), and cloud top temperature (e, f). The linear trends (± uncertainty) are indicated with the solid lines (shared area is 95% confidence interval) and trend values in units per decade, the coefficient of determination r^2, and χ^2 are presented in legend.

to La Niña events (negative ENSO in 2020 to 2022). Similar patterns can be observed for CTT, δ_h, etc., or even with a certain difference in phase (e.g. CBH) and varying intensity of the oscillation.

Since no absolute certainty can be obtained about which single or combination of climate modes are modulating the MPC observations, three common indices are considered, namely: Arctic Oscillation (AO), PDO, and ENSO. In Eq. 4b the free parameter ν_k (frequency of signal) was selected among a set of frequencies from relevant harmonics of these three climate indices. The set of values for ν_k was obtained after a discrete Fourier analysis performed over the ENSO, PDO and AO signals (details in App. D). Only frequencies associated with strong Fourier components (amplitudes larger than 100) were considered to be relevant (red triangles over the x-axis of Fig. D1 (c) in App. D): ν_k={0.093, 0.155, 0.186, 0.217, 0.248, 0.279, 0.341, 0.434} yr^{-1} which corresponds to periods of {10.8, 6.5, 5.4, 4.6, 4.0, 3.6, 2.9, 2.3} yr, values in agreement with other more extensive analysis i.e. 2.8, 4.3, and 5.7 yr period for AO, plus 12 yr for ENSO (Zhang and Moore, 2011). All ν_k values are common harmonics for ENSO, PDO and AO, albeit with various levels of contribution to the climate indices. The time series are fitted to Eq.4b using all values of ν_k (e.g. six fitted curves), and the three goodness of fit parameters are calculated, namely χ^2, coefficient of determination r^2, and the normalized root mean square error nRMSE. Then the best ν_k is determined by minimizing a cost function (Eq. A5) dependent of χ^2, r^2, and nRMSE. The corresponding parameter definitions and description of the procedure can be found in Appendix A1 and Fig. A1 for LWP and CTT as examples.

The time series of MPC properties fitted to Eq. 4b to obtain the coefficients $\boldsymbol{\beta}$ are shown in Fig. 8 for H-pressure systems, while the cases for L-pressure systems are presented in Appendix Fig. B1. The fitting to Eq. 4b is performed for all values of ν_k, then a single frequency ν_k is selected based on the goodness of fit test (shown as legend in Fig. 8) which, along with the set of $\boldsymbol{\beta}$ parameters, represents the best fit for the data (dashed-lines in Fig. 8).

From Fig. 8 (a) and (b) it can be seen that under H-pressure systems, decoupled LWP is better represented by a cyclical signal with a period of 6.5 years, while coupled LWP by 10.8 years. That difference in periods together with the amplitude coefficients $\boldsymbol{\beta}$, fitted to Eq. 4b in each case, yield to dissimilar trends ($\frac{\Delta}{\Delta t} \equiv \beta_2$ in Eq. 4b) for decoupled (-0.9$\pm$0.9 $\mathrm{g\,m^{-2}\,dec^{-1}}$) and coupled (+8.0$\pm$0.7 $\mathrm{g\,m^{-2}\,dec^{-1}}$) cases. Moreover, based on the Fourier transform analysis of the climate indicators, the period of 6.5 year suggest that decoupled LWP is likely linked to AO and PDO while the coupled LWP has a stronger modulation by harmonics of ENSO and PDO.

The liquid layer cloud base height CBH for wintertime MPC (Fig. 8 c and d) shows a best fit for periodic signal with periods of 3.6/6.5 years for decoupled/coupled, respectively. For decoupled cases, a negative CBH trend was found: -228.1$\pm$1.5 $\mathrm{m\,dec^{-1}}$. Contrarily, for coupled cases a positive liquid CBH trend of +119.9$\pm$0.7 $\mathrm{m\,dec^{-1}}$ was found. Concerning cloud top temperature CTT (Fig. 8 e and f) a slightly positive, albeit not statistically significant trend is found for both decoupled: +0.7$\pm$1.0 $\mathrm{K\,dec^{-1}}$, and coupled: +0.4$\pm$0.6 $\mathrm{K\,dec^{-1}}$) cases, with good fit to periods of 5.4 and 10.8 years respectively. From the three climate indices analysed in Appendix D, the period of 10.8 years is intelligibly present in the PDO and ENSO power spectra, with the strongest component belonging to PDO. A period of 5.4 years is the strongest signal for the intra-decadal ENSO variability, and the second strongest for PDO, while non-present for AO.

3.2.3 Comparison of trends obtained by the two methods

The results for trends presented in Sec. 3.2.1 and Sec. 3.2.2 have been estimated considering data for all SIC conditions above zero. Additionally, the same procedure was performed considering subsets of SIC comprised by the lower and upper 50th

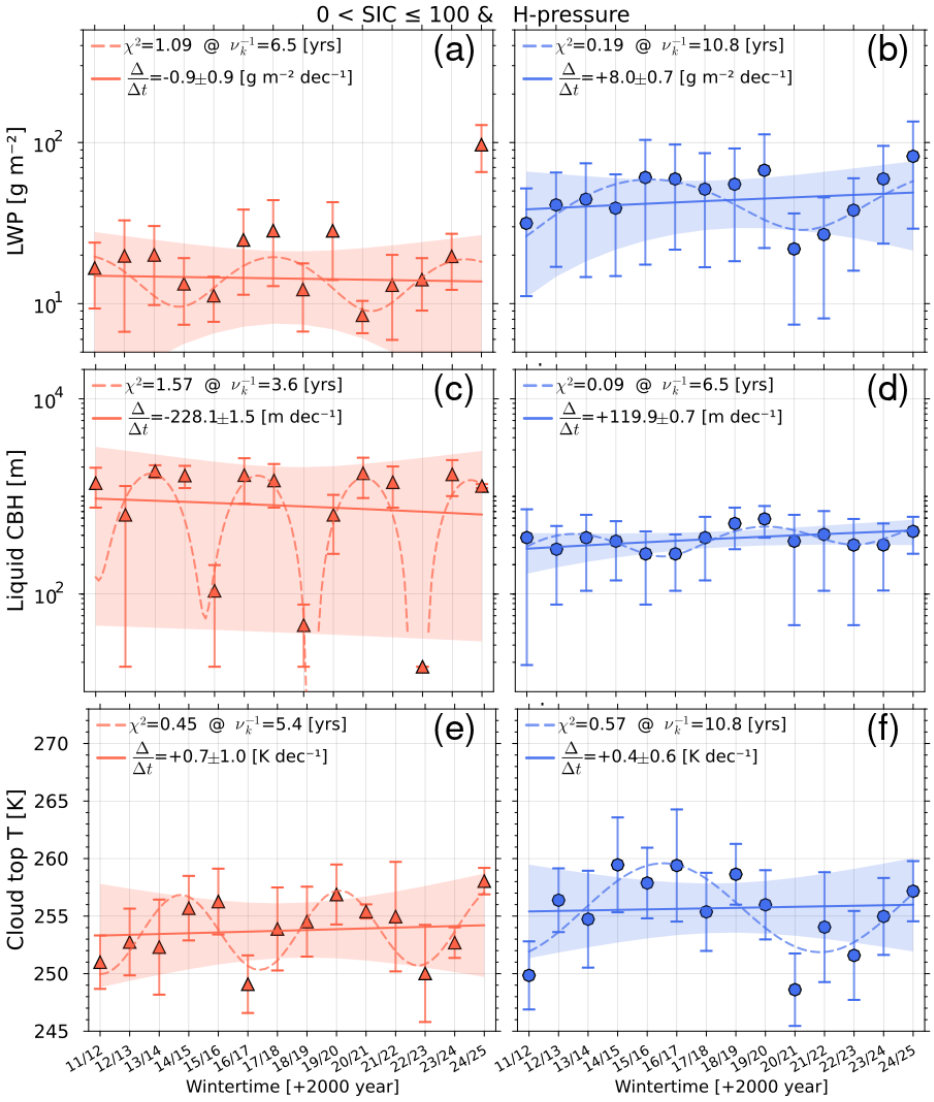


Figure 8. Same as in Fig. 7 but applying method *ii* for H-pressure systems. With LWP (a) and (b), liquid layer CBH (c, d), and CTT (e, f). Left column panels (a,c,e) show decoupled MPC (orange triangles) cases and right column (b,d,f) coupled MPC cases (blue circles). The best fit curves are dashed-lines and linear trends are the solid lines (shared area is 95% CI). The goodness of fit coefficient χ^2, the period of the cyclical curve ν_k^{-1}, and trend values, in units per decade, are indicated in legend.

percentiles of the total distribution of SIC. Those quantiles translate to two bins of SIC, i.e. the set of SIC = { (0, 95], (95, 100] }%, for which their corresponding trends were estimated. Here the notation of, for example (0, 95], indicates that only data with 0%<SIC≤95% was used to perform the procedures shown in previous sections.

In Fig. 9 the set of LWP trends as a function of SIC subset is summarized. The SIC on the-axis indicated as "All" corresponds to the results shown in Fig. 7 and Fig. 8. The coupled cases are presented on the top row of panels in Fig. 9 (a and b), while the

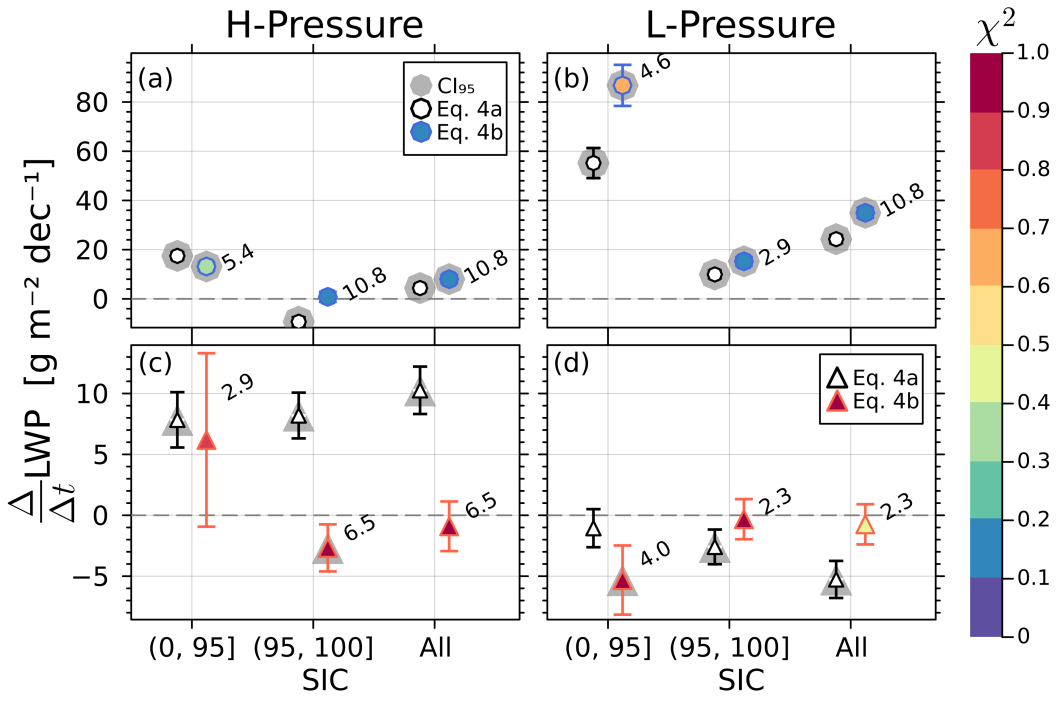


Figure 9. LWP trends for SIC subsets as indicated in the abscissae. The hollow symbols indicate the trend using method *i* (Eq. 4a), coloured symbols show results using method *ii* (Eq. 4b), grey shadows behind symbols indicate the trend is statistically significant (p<0.05), and the number next to the coloured symbols are the period in years for the best fit Eq. 4b. The colour bar represents the goodness of fit χ^2 value. MPC observed in the presence of H-pressure systems in panel (a) and (c) for coupled and decoupled cases, respectively. MPC in the presence of L-pressure systems in panels (b) and (d) for coupled (upper row) and decoupled (lower row) cases, respectively.

decoupled cases on the bottom row (c and d). The trends estimated using Eq. 4a (method *i*) are hollow symbols, whereas the trends estimated fitting Eq. 4b (method *ii*) are the coloured symbols where the colour indicates the goodness of fit parameter χ^2 (the lower the value the better the fit). Next to every coloured symbol the period related to the best fit ν_k^{-1} in Eq. 4b is indicated.

It is noticeable from panel a and b in Fig. 9, that with respect to MPC-LWP the coupled clouds' trends agree between the two methods, especially for SIC>95% (50th percentile), while for SIC<95% the two methods start showing differences with an extreme value of ≈+55 and ≈+86 $\mathrm{g\,m^{-2}\,dec^{-1}}$ for SIC within the lower 50th percentile under L-pressure for methods *i* and *ii*, respectively. Most of the LWP trends in the coupled cases follow time series oscillation with periods of 4.6, 5.4, and 10.8 years, characteristics for PDO and ENSO oscillations.

On the contrary, for the decoupled clouds (panels c and d in Fig. 9)) a large variability of the trend values was found. Specifically for method *ii*, trends were found to reverse sign from positive to negative as the SIC increases when H-pressure systems are present over NSA site. LWP-trends for MPC in decoupled situations and under L-pressure system were slightly

negative for both methods and low and high SIC (Fig. 9 d).The oscillation periods for decoupled cases are dominated mainly by AO and ENSO signals (i.e. 2.3, 2.9, 4.0, 6.5 years) and thus somewhat shorter than for coupled cases.

Regarding ice cloud properties, IWP of coupled clouds does not have a statistically significant trend at L-pressure conditions, similarly Ice r_{eff} does not show any significant trend (Fig. S2 (b, c, d)) when the moving average method is used. IWP only has a significant trend when the method *ii* is used for trend determination. In that case IWP exhibits a positive trend at L-pressure affected by a 2.9 years oscillation e.g. ENSO (Fig. S5 (b)), and at H-pressure a 10.8 years oscillation e.g. ENSO/PDO (Fig. S4 (b)). This suggest effects on cloud properties are likely due to weather patterns and intrusions of warm air from low latitudes, a similar conclusion was found by Cesana et al. (2024) for the Bearing Sea using satellite observations.

3.3 Discussion

The findings presented in this study are the result of two approaches: first, an extension of the PSG23 method from one winter of observations during the MOSAiC expedition in the Central Arctic to multi-year observations within the Western Arctic (in Sec. 3.1); and second, the multi-year time series analysis of the MPC properties (Sec. 3.2). To account for this, the following discussion is split based on results reported in this study set into context with the MOSAiC expedition, and the results from the time series analysis.

On the MPC properties modulated as a function of SIC, coupling status, and pressure system

Section 3.1 along with Fig. 5 and Fig. 6 are only partially comparable to the findings reported by PSG23 for the MOSAiC expedition. As previously mentioned, this is because the MOSAiC study mainly relies on the sea ice lead fraction (LF) to represent the sea ice states. Contrarily, for the present study, long-term and continues LF data are not available. Furthermore, SIC MOSAiC winter was mostly above 90% while during the 14 years of Nov-April observations at NSA site considered here, a large variation in SIC was covered. Keeping these caveats in mind, the following phenomena reported by Saavedra Garfias et al. (2023) can be confirmed:

- LWP of coupled wintertime MPC increases as the sea ice states trend to larger openings, whereas decoupled LWP has no relationship with SIC. The present study thus confirms MOSAiC findings and extends its validity for SIC as low as 5%.
- Cloud layers for coupled cases are thicker and have a lower liquid layer base height than the decoupled cases.
- The temperature lapse-rate within the cloud layer (Γ_{cloud}) for coupled cases and SIC>95% is distributed from negative to positive values while decoupled cases have a distribution predominantly above zero. For SIC<95% Γ_{cloud} increases with increasing sea ice opening for both coupled and decoupled clouds.

Conversely, new findings that the study from the MOSAiC expedition did not conclude (e.g. because no distinction between pressure system was made there) can be summarized as follows:

- Coupled liquid cloud base height is lower than for the decoupled cases for L-pressure systems and all SIC. For H-pressure systems that is only evident for SIC$\gtrsim$95%.
- A negative relationship between IWP and SIC was found, albeit only for coupled MPC~~for H-pressure/L-pressure cases~~.
- The liquid and ice effective radii (r_{eff}), which Saavedra Garfias et al. (2023) reported not to present a clear difference when sorted by coupled status or lead fraction, was found to have a strong dependency on SIC for coupled cases. Specifically, r_{eff} were found to increase with decreasing SIC.
- For coupled MPC, negative Γ_{cloud} (in-cloud temperature inversion) at SIC>95% is possible. For low SIC values the Γ_{cloud} >0, i.e. a tendency towards a moist adiabatic lapse-rate is observed. Decoupled Γ_{cloud} cases exclusively show a moist adiabatic lapse-rate enhancing in magnitude as SIC reduces, especially for L-pressure systems.

On the long-term trends of MPC properties

The application of two methods for trend estimation has shown a dependency of results based on the specific procedure adopted for trend estimation. Although method *i* is a standard procedure for signals with stochastic variability or well-known periodicity, its biggest limitation is the sensitivity to the edges and the width of moving average window. That is especially the case for finite oscillatory signals, where the time series' cut-off edges produce the average window to be either overestimated (signal crest) or underestimated (signal trough). Disagreements in the method's results refer to the magnitude of the trends and the tendency of change. For instance, for L-pressure trends of LWP of decoupled MPC differ considerably from method *i* (-5.3$\pm$0.7 $\mathrm{g\,m^{-2}\,dec^{-1}}$) versus method *ii* (+0.9$\pm$0.9 $\mathrm{g\,m^{-2}\,dec^{-1}}$). The underlying reason for that is that for all time-series method *i* uses a constant moving window size, whereas the best cyclical signal fit suggests a period of 6.5 years which is much lower than the window size (10 years), thus method *i* oversmooth the time series.

An example of tendency disagreement occurs for the liquid cloud base height of decoupled MPC, where method *i* results in a positive trend of +54.9$\pm$1.0 $\mathrm{m\,dec^{-1}}$ in contradiction to method *ii* with a negative trend of -228.1$\pm$1.5 $\mathrm{m\,dec^{-1}}$, both statistically significant. Figure 8 (c) shows how method *ii* favours a periodic signal of 3.6 years to properly fit the low CBH values observed during negative ENSO phases (e.g. 2018/19, 2022/23), whereas method *i* with an average window of $\pm$5 yr smoothes out these low CBH observations.

The IWP (shown in supplementary material S2.2) for H-pressure shows a remarkable agreement of both methods, with a trend for coupled cases of +3.5$\pm$0.8 $\mathrm{g\,m^{-2}\,dec^{-1}}$ and +4.4$\pm$1.0 $\mathrm{g\,m^{-2}\,dec^{-1}}$ for method *i* and *ii*, respectively, at a signal period of 10.8 years (characteristic for ENSO and PDO).

The assumption that climate modes variability might modulate the observed oscillatory nature of MPC properties has been tested by fitting the data to Eq. 4b with one relevant harmonic as a free parameter ν_k. In other words, the NSA site observations' time series can be explained by the ENSO, PDO, or AO characteristic intra-decadal periods. Among the values of ν_k, it has been found that the PDO and ENSO period of 10.8 or 5.4 years are representative for the fluctuation of several MPC parameters. The ENSO and AO period of 2.3 and 2.9 years are the second most frequent. AO and PDO's period of 6.5 has additionally been found among the best fits. In summary, properties of decoupled MPC under H-pressure influence vary within middle range

periods (3.6, 4.0, 5.4 years), while coupled MPC variation in on longer periods (6.5, 10.8 years). Conversely, the variability of decoupled MPC L-pressure cases is mostly found at 2.3 to 6.5 years, while properties of coupled MPC cases mostly oscillate at 2.9, and 10.8 years, depending on the specific MPC property.

4 Conclusions

The method proposed by Saavedra Garfias et al. (2023) to study the relationships of atmospheric boundary layer MPC properties coupled to sea ice leads during the MOSAiC expedition in the central Arctic has been successfully implemented and extended to the Western Arctic. Fourteen winter seasons of multi-sensor synergistic observations by the ARM's NSA site were analysed to characterize MPC properties along with space-borne observed sea ice conditions. We found a remarkable relationship between the reduction of sea ice concentration and an increase of some MPC properties such as LWP, effective radius of cloud droplets and ice particles effective, and cloud top temperature (CTT).

The MOSAiC expedition's systematic difference between MPC properties belonging to clouds coupled or decoupled via the water vapour transport-sea ice system has been confirmed for the NSA site. Additionally, the multi-year dataset allowed to study the influence of the weather pressure system in which the observation took place. We found that some MPC properties can increase or decrease in magnitude depending not only on their coupling status but also as a function of the atmospheric weather pressure system. Conclusive is that for L-pressure systems the long-term rate of change for LWP, cloud top temperature, and liquid layer base height in wintertime MPC is positive for coupled cases. For decoupled cases, no trend in LWP and CTT was detectable while liquid layer base height was found to decrease. When H-pressure systems are considered, mostly the same tendency of change in wintertime MPC properties was found albeit with different magnitudes.

We applied two methods to estimate the rate of change of MPC properties and found that the method used plays a decisive role: the estimated time series trends were found to depend on which methods was applied. Furthermore, we discovered that Arctic wintertime MPC properties fluctuate over time analogous to oscillations of Arctic relevant climate modes, like ENSO, PDO, or AO. This commonality permits the exploitation of known ENSO or PDO frequencies of oscillation to physically constrain the detected undulating nature of MPC properties~~, thereby~~. Although trends are accurately estimated, the robustness of statistically significant trends will be strengthen as more years of observations will modify or confirm the significance of our results. We found that properties like LWP, CTT, and surface skin temperature show features that resemble ENSO cycles, with maxima/minima for years characterized by El Niño/La Niña events, respectively. Based on time series of surface skin temperature as indicator of coupled clouds radiative feedback, we found that a continuing warming in the Western Arctic can only be reckoned under a L-pressure system linked to observations with SIC<95%. Contrarily, under high pressure systems and SIC≥95%, our results show that the cloud radiative induced surface temperature is decreasing. A limitation of this study is that the current NSA site remote sensing capabilities does not provide vertical profile information about aerosols which hinders the study of the effects of aerosols to LWP and IWP in conjunction to SIC changes.

This study put into consideration empirical mathematical models derived from long-term observations as parameterization for the modelling of atmospheric boundary layer MPC ascribed to Arctic sea ice conditions. We suggest that the sea ice-

atmospheric feedback processes that are represented in Arctic weather and climate models certainly should aim to mirror the complexity of relationships that the present study has uncovered. This implies the consideration of not only small-scale horizontal moist air mass transport that serves as physical link between sea ice openings and clouds downstream, but also weather patterns, large-scale atmospheric circulation processes, intra- and multi-decadal climate oscillations, and teleconnections between the Arctic and lower latitudes. Recent studies reported that this complexity has implications for the prospect of decadal climate predictability (Timmermann et al., 2018; Mann et al., 2020; Cesana et al., 2025). Similar findings were recently reported by Lubin et al. (2026). They analysed LWP and CRE trends from 1999 to 2024 and reported an influence by large scale circulation and atmospheric rivers in long-term trends. With this study we acknowledge the immense importance of long-term stations like the ARM NSA site for the continuous monitoring of the Arctic which made this study possible.

Code and data availability. Code and data available at Saavedra Garfias and Kalesse-Los (2022) and references listed in Table 1.

Appendix A: Statistical parameters used in the data analysis

The statistics for cloud properties are represented by the geometric mean, median or 1st and 3rd quantile. The variability within the distribution is expressed by the standard deviation (σ_g) or MAD (σ_{mad}). When the data mean or median is used to fit an analytical model, the variability within the distribution is taken into account by performing a weighted fitting either by linear or non-linear regression. The weights are modelled as

$$\omega_j = \frac{\sigma_j^{-2}}{\langle \sigma_j^{-2} \rangle} \tag{A1}$$

with σ_j^{-2} is the inverse of the variance (with σ_j can be σ_g or σ_{mad}), and $\langle \sigma_j^{-2} \rangle = \frac{1}{N} \sum_j \sigma_j^{-2}$ is the inverse variance mean. The index j represents a distribution of cloud properties, which for the case of Sec. 3.1 $j \in SIC = \{10, 20, \ldots, 100\}$ is the distribution within binned sea ice concentration, and for the case of Sec. 3.2 $j \in WT = \{2011/12, \ldots, 2024/25\}$ for the wintertime. In both cases N is the length of j set. The Eq. A1 penalize large variability within the distribution j and will influence less the fitting algorithm.

A1 Model Goodness of fit test

To quantify the degree of a fitted model can represent the observations, the following parameters for goodness of fit are used:

- χ^2: is the sum over residuals square divided by the fitting model degrees of freedom ν, which indicates how close the model prediction is from the data,

$$\chi^2 = \frac{1}{\nu} \sum_{j=1}^{N} \left(\frac{\varepsilon_j}{\sigma_j} \right)^2 \tag{A2}$$

where $\varepsilon = \hat{y_j} - y_j$ are the residuals (difference between model prediction $\hat{y_j}$ and observed value y_j) in Eq. 3, Eq. 4a, and Eq. 4b; with ν =2, 2, and 4, respectively. The closer χ^2 is to zero, the better the fir curve represent the data.

- r^2: is the coefficient of determination, which quantifies how good the model explains the change in observed value,

$$r^2 = 1 - \frac{\sum\limits_j \varepsilon_j^2}{\sum\limits_j (\langle y_j \rangle - y_j)^2} \tag{A3}$$

where $\langle y_j \rangle$ is the average over all observed values y_j. Worth to note that r^2 is generally a valid parameter for linear relationships, while for non-linear regression it could produce unexpected results like negative values or larger than one (Spiess and Neumeyer, 2010).

- nRMSE: is the normalized root mean square error, which is the overall mean squared residual between model fitted and observed value,

$$\text{nRMSE} = \frac{\sqrt{\frac{1}{N}\sum\limits_j (\omega_j^2 \varepsilon_j^2)}}{\text{IQR}} \tag{A4}$$

with IQR is the distribution inter-quantile region, and ω_j the weights as in Eq. A1. Values of nRMSE larger than one signalize a very poor agreement between fitted model and observations.

Given a set of fitted parameters to Eq.4b corresponding to the six ν_k values, a goodness of fit test is performed to determine which single ν_k represents the data the best. This is done by minimizing a cost function which is dependent of all three goodness of fit parameter χ^2, nRMSE, and the reciprocal of r^2 i.e. 1-r^2, thus all three parameters range from zero (best) to higher values (worst):

$$\mathcal{L} = \sqrt{\chi^2 + \text{nRMSE}^2 + (1 - r^2)} \tag{A5}$$

As an example of how the minimum is found, in Fig. A1 can be seen the cost function for two MPC parameters: LWP and CTT, with the minimum of the cost function $\mathcal{L}$ indicated by the vertical thick line.

Appendix B: Results for trend estimation

To complement Sec. 3.2.2, the equivalent of Fig. 8 but for L-pressure systems is shown in Fig. B1 with LWP in panels (a) and (b), liquid CBH in panels (c) and (d), and cloud top temperature in panels (e) and (f). Further results of time series trends of other MPC properties can be found in the supplementary material.

B1 Time series for the lower/upper 50th percentile SIC decomposition

The time series' trend analysed by method *ii* are decomposed by the lower and upper 50th percentile of sea ice concentration. For the period of 14 years observations the lower 50th percentile comprises of data with SIC between 0% and 95%, whereas the upper half from SIC above 95% to 100%. Figure B2 shows the LWP SIC decomposition.

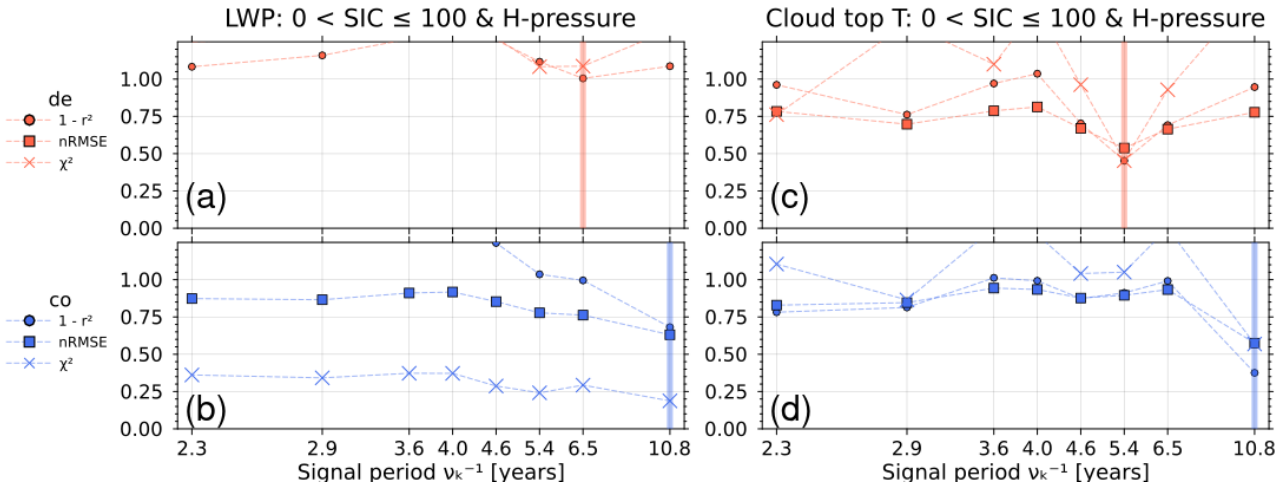


Figure A1. Determination of the best ν_k value, from the combination of all three goodness of fit parameters. LWP coupled (a) and decoupled (b), cloud top temperature coupled (c) and decoupled (d). The χ^2 is shown as crosses, nRMSE as squares, and the reciprocal of r^2 as circles. The thick vertical line is the value of ν_k that minimizes the cost function $\mathcal{L}$.

B2 Surface skin temperature trend results after SIC decomposition

Time series analysis for the surface skin temperature T_{skin}, estimated from the net down- and up-welling longwave radiation flux (Saavedra Garfias et al., 2024), or by down-welling infrared radiometer when the former data is not available, after being decomposed in SIC subsets of 50th percentiles (shown in Sec. S2.3, Fig. S8) applied to methods in Sec. 3.2.1 and Sec. 3.2.2 are displayed in Fig. B3. These results are discussed in Sec. 3 in relation to the warming in the western Arctic.

Appendix C: Sensitivity to radius of semi-circle around NSA site for SIC parameter

To investigate how sensitive the results are to the choice of sea ice area (red cone in Fig. 1) to compute the average SIC associated to be coupled/decoupled to the MPC parameters, in addition to the 50 km used for the results in Sec. 3, a different radius o´f 75 km has been tested. The procedure indicated in Sec. 2 was repeated for 75 km and the results for LWP trend are summarized in Table C1 as compared to the results for 50 km. It has been found that there is a small difference between results from 50 km and 75 km radius (second column in Table C1), but the differences are more noticeable for decoupled cases in particular when grouped to 0≤SIC<95%.

In supplementary material (Sec. S3) the associated Figure for 75 km radius around NSA site can be found. A noticeable difference is mostly seen for the results associated to decoupled cases and SIC between 0 and 95%. For coupled cases the results are robust and consistent either by selecting SIC within 50 or 75 km.

Appendix D: Frequency decomposition for climate indicators

A discrete Fourier analysis has been performed to obtain the frequency harmonics ν_k from three climate indicators: Arctic oscillation (AO), Pacific Decadal Oscillation (PDO), and El Niño Southern Oscillation (ENSO). The power spectrum as a function of the signal harmonics expressed as periods (ν_k^{-1}) is shown in Fig. D1, with the set of harmonics used to test the fitting of Eq. 4b indicated by a red triangle at the bottom of panel (c) in Fig. D1. Note that the limits of the abscess in Fig. D1 is intentionally cut for the range relevant to the 12 year of observation period, the signal can contain multi-decadal harmonics that excesses the 12 years period.

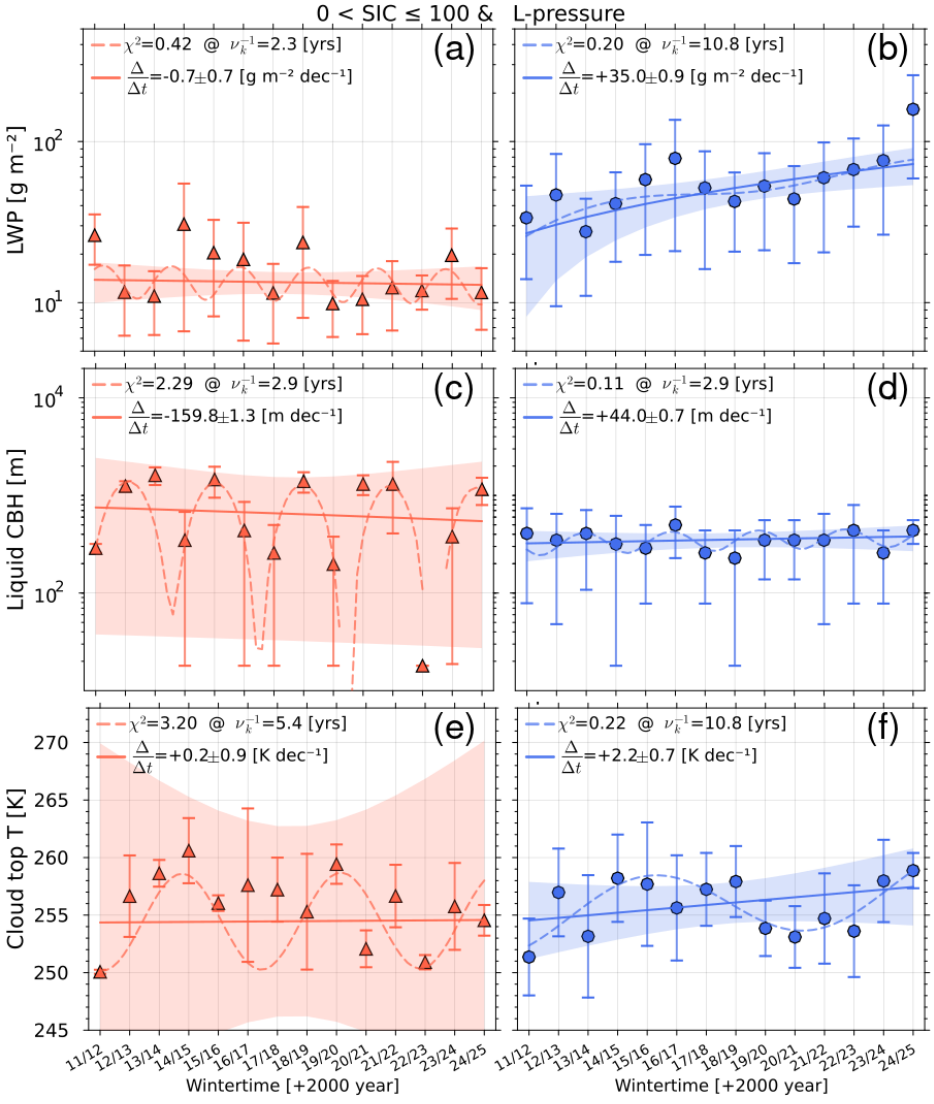


Figure B1. Same as in Sec. 3.2.2, Fig. 8 but for time series comprised of L-pressure systems.

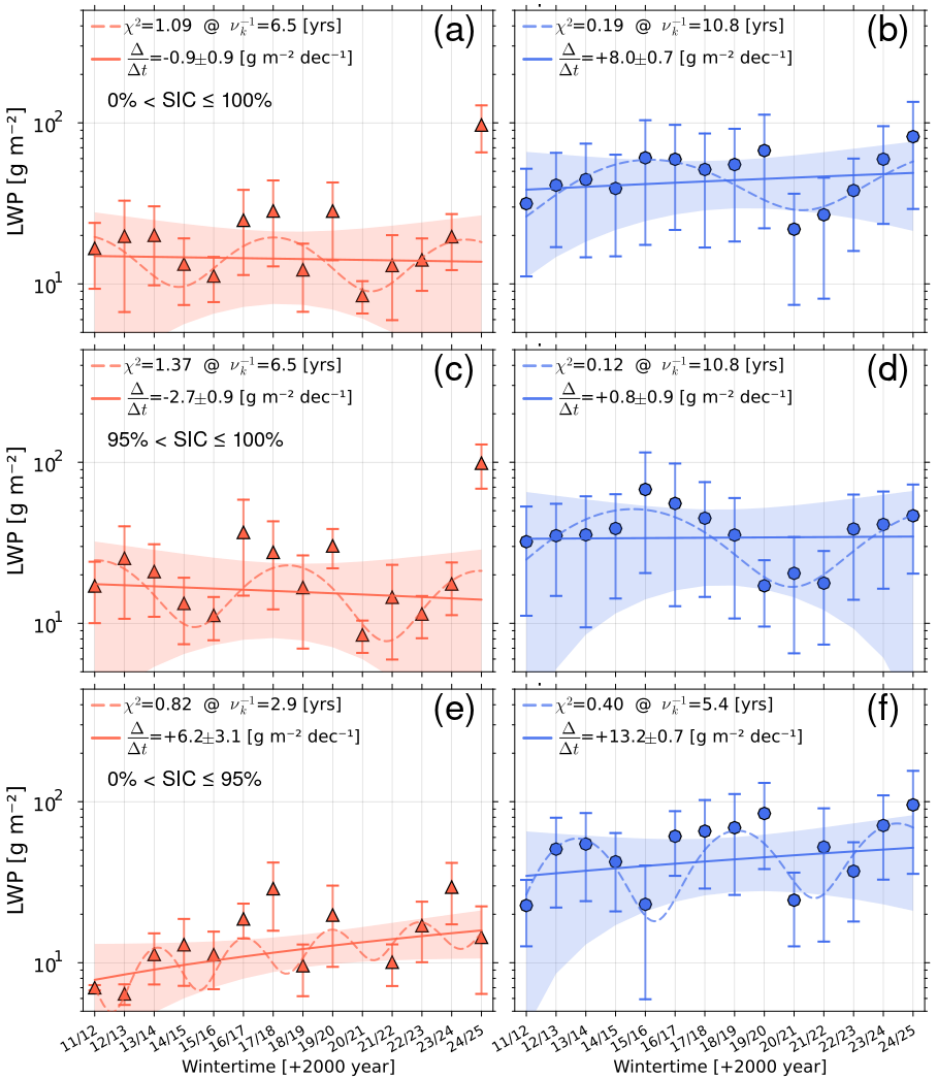


Figure B2. Time series of LWP for coupled and decoupled clouds under H-pressure systems. The time series are decomposed by the range of SIC: (a) and (b) all SIC considered, (c) and (d) for SIC > 95% and SIC $\leq$ 100%, and (e) and (f) for SIC > 0% and SIC $\leq$ 95%.

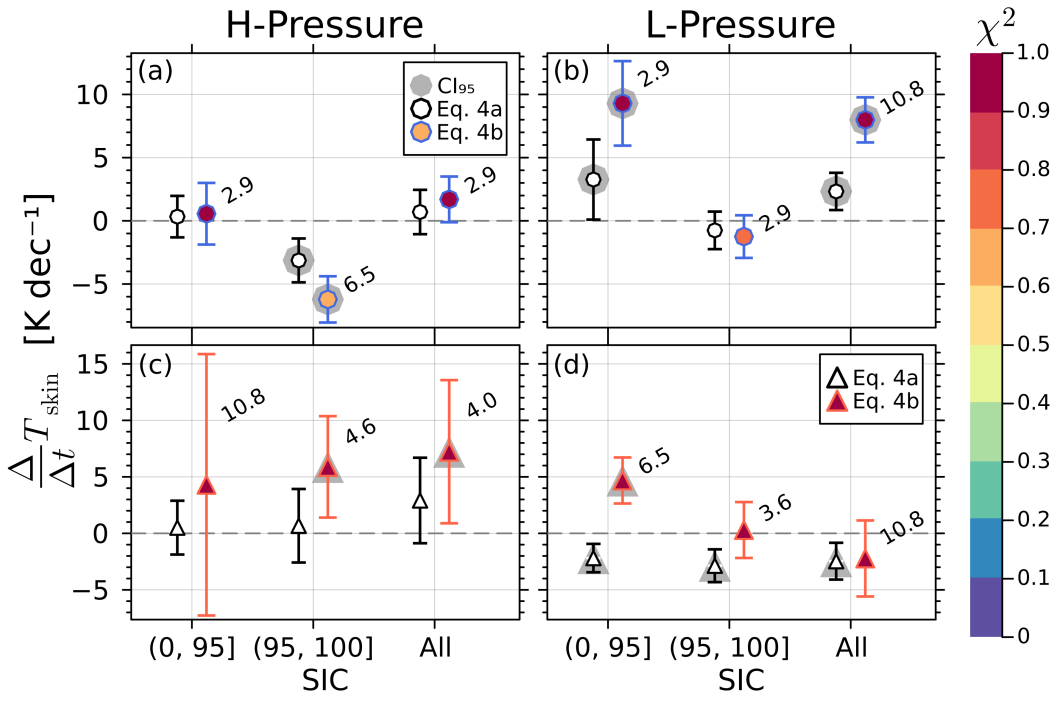


Figure B3. T_{skin} rate of change for SIC subsets in the abscissae. The hollow symbols are trends using method *i* (Eq. 4a), coloured symbols use method *ii* (Eq. 4b), grey shadows behind symbols indicate the trend is statistically significant (p<0.05), and the number next to the coloured symbols is the period in years for the best fit Eq. 4b. The colour table represents the goodness of fit χ^2 value. H-pressure systems in panel (a) and (c) for coupled and decoupled cases. L-pressure systems in panels (b) and (d) for coupled and decoupled, respectively.

Table C1. Comparison for 2011 to 2024 wintertime LWP trends when considering SIC within two sectors of radius 50 km or 75 km.

High Pressure systems ($\Delta Z < 0$)								
SIC	R_{sic}	Decoupled			Coupled			Reference
[%]	[km]	χ^2	ν_k^{-1} [yrs]	$\frac{\Delta}{\Delta t}$LWP [$g\,m^{-2}\,dec^{-1}$]	χ^2	ν_k^{-1} [yrs]	$\frac{\Delta}{\Delta t}$LWP [$g\,m^{-2}\,dec^{-1}$]	figure
0–100	50	1.09	6.5	-0.9 ± 0.9	0.19	10.8	+8.0 ± 0.7	8 (a, b)
	75	1.26	2.3	-3.2 ± 1.3	0.17	10.8	+10.2 ± 0.7	S13 (a, b)
95–100	50	1.37	6.5	-2.7 ± 0.9	0.12	10.8	+0.8 ± 0.9	B2 (c, d)
	75	1.44	6.5	-6.9 ± 1.2	0.15	10.8	+0.1 ± 0.8	S13 (c, d)
0–95	50	0.82	2.9	+6.2 ± 3.1	0.40	5.4	+13.2 ± 0.7	B2 (e, f)
	75	1.30	2.3	-24.0 ± 1.2	0.39	2.3	+21.8 ± 1.0	S13 (e, f)
Low Pressure systems ($\Delta Z > 0$)								
SIC	R_{sic}	Decoupled			Coupled			Reference
[%]	[km]	χ^2	ν_k^{-1} [yrs]	$\frac{\Delta}{\Delta t}$LWP [$g\,m^{-2}\,dec^{-1}$]	χ^2	ν_k^{-1} [yrs]	$\frac{\Delta}{\Delta t}$LWP [$g\,m^{-2}\,dec^{-1}$]	figure
0–100	50	0.42	2.3	-0.7 ± 0.7	0.20	10.8	+35.0 ± 0.9	S8 (a,b)
	75	0.49	3.6	+0.3 ± 0.7	0.21	10.8	+34.3 ± 0.9	S12 (a, b)
95–100	50	0.94	2.3	-0.3 ± 0.7	0.13	2.9	+15.3 ± 0.8	S8 (c,d)
	75	1.35	2.9	+1.3 ± 0.6	0.11	2.9	+17.6 ± 0.7	S12 (c, d)
0–95	50	1.37	4.0	-5.4 ± 1.3	0.64	4.6	+86.8 ± 3.7	S8 (e,f)
	75	1.13	2.9	+3.3 ± 17.9	0.32	4.6	+79.9 ± 0.8	S12 (e, f)

Appendix E: List of Acronyms and variables

Acronym	Description
AMSR2	Advanced Microwave Scanning Radiometer 2
AO	Arctic Oscillation
ASI	Arctic sea ice algorithm
CEIL10m	Ceilometer 10 m resolution
CRE	Cloud Radiative Effect
ENSO	El Niño Southern Oscillation
INTERPSONDE	Interpolated Radiosonde
KAZR	Ka Zenith Radar
MPC	Mixed-phase Clouds
NSA	North Slope of Alaska
MWR	Microwave Radiometer
PDO	Pacific Decadal Oscillation

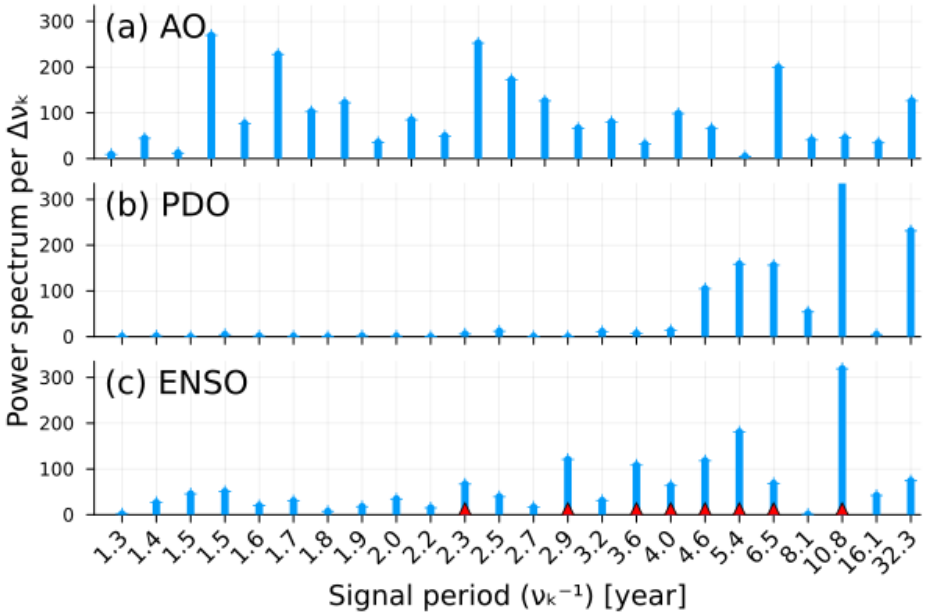


Figure D1. Power spectrum per frequency bandwidth for three climate indicators: (a) Arctic Oscillation, (b) Pacific Decadal Oscillation, (c) El Niño Southern Oscillation. The relevant frequencies are indicated by red triangles at the bottom of panel (c). Note, the peak at 10.5 year in panel (b) is cut at 300 for comparison reasons.

Symbol	Description	Unit
LWP	liquid water path	$\mathrm{g\ m^{-2}}$
IWP	ice water path	$\mathrm{g\ m^{-2}}$
∇_zWVT	vertical gradient of water vapour transport	$\mathrm{kg\ m^{-2}\ s^{-1}}$
CBH	liquid cloud base height	m
CTH	cloud top height	m
CMLH	cloud mixing-layer height	m
CTT	cloud top temperature	K
SIC	sea ice concentration	%
Ze	radar equivalent reflectivity factor	dBz
β	lidar attenuated backscattering coefficient	$\mathrm{m^{-1}\ sr^{-1}}$
P	atmospheric pressure	Pa
q_v	specific humidity	$\mathrm{g\ g^{-1}}$
$\boldsymbol{v}_w$	horizontal wind speed	$\mathrm{m\ s^{-1}}$
W_d	wind direction from North	°
θ_v	virtual potential temperature	K
Ri_b	bulk Richardson number	-
T_{skin}	skin surface temperature	K
Γ_{cloud}	cloud layer temperature lapse rate	$\mathrm{K\ km^{-1}}$
r_{eff}	cloud layer average effective radius	μm

Author contributions. PSG conceptualized the research idea, performed the data processing, and analysis of results. HKL conceptualized the research idea, provided advise and supervision. Both authors were involved in the manuscript preparation.

Competing interests. No competing interests.

Acknowledgements. Our gratitude to the DOE ARM program for openly provide the data from its North Slope of Alaska site in Utqiagvik Alaska, and to the open Sea Ice data repository from the University of Bremen. We gratefully acknowledge the funding by the Deutsche Forschungsgemeinschaft (DFG, German Research Foundation) - Projektnummer 268020496 - TRR 172, within the Transregional Collaborative Research Center "ArctiC Amplification: Climate Relevant Atmospheric and SurfaCe Processes, and Feedback Mechanisms (AC)3". This work was funded by the Open Access Publishing Fund of Leipzig University supported by the DFG within the program Open Access Publication Funding. We acknowledge ACTRIS and Finnish Meteorological Institute for providing the data set which is available for download from https://cloudnet.fmi.fi. We acknowledge ECMWF for providing IFS model data.

References

Andreas, E. L. and Cash, B. A.: Convective heat transfer over wintertime leads and polynyas, Journal of Geophysical Research: Oceans, 104, 25 721–25 734, https://doi.org/10.1029/1999JC900241, _eprint: https://onlinelibrary.wiley.com/doi/pdf/10.1029/1999JC900241, 1999.

Arrhenius, S.: On the influence of carbonic acid in the air upon the temperature of the Earth, Publications of the Astronomical Society of the Pacific, 9, 14, https://doi.org/10.1086/121158, publisher: IOP Publishing, 1897.

Cadeddu, M., Morris, V., and Tuftedal, M.: Microwave Radiometer (MWRLOS), https://doi.org/10.5439/1999490, last access: 30 April, 2024.

Cesana, G. V., Pierpaoli, O., Ottaviani, M., Vu, L., Jin, Z., and Silber, I.: The correlation between Arctic sea ice, cloud phase and radiation using A-Train satellites, Atmospheric Chemistry and Physics, 24, 7899–7909, https://doi.org/10.5194/acp-24-7899-2024, 2024.

Cesana, G. V., Roach, L. A., and Blanchard-Wrigglesworth, E.: Clouds Are Crucial to Capture Antarctic Sea Ice Variability, Geophysical Research Letters, 52, e2024GL113 322, https://doi.org/https://doi.org/10.1029/2024GL113322, e2024GL113322 2024GL113322, 2025.

Chang, K.-L., Schultz, M. G., Lan, X., McClure-Begley, A., Petropavlovskikh, I., Xu, X., and Ziemke, J. R.: Trend detection of atmospheric time series: Incorporating appropriate uncertainty estimates and handling extreme events, Elementa: Science of the Anthropocene, 9, 00 035, https://doi.org/10.1525/elementa.2021.00035, 2021.

Cox, C. J., Walden, V. P., Rowe, P. M., and Shupe, M. D.: Humidity trends imply increased sensitivity to clouds in a warming Arctic, Nature Communications, 6, 10 117, https://doi.org/10.1038/ncomms10117, publisher: Nature Publishing Group, 2015.

Deng, J. and Dai, A.: Arctic sea ice–air interactions weaken El Niño–Southern Oscillation, Science Advances, 10, eadk3990, https://doi.org/10.1126/sciadv.adk3990, 2024.

Griesche, H. J., Seifert, P., Ansmann, A., Baars, H., Barrientos Velasco, C., Bühl, J., Engelmann, R., Radenz, M., Zhenping, Y., and Macke, A.: Application of the shipborne remote sensing supersite OCEANET for profiling of Arctic aerosols and clouds during *Polarstern* cruise PS106, Atmospheric Measurement Techniques, 13, 5335–5358, https://doi.org/10.5194/amt-13-5335-2020, 2020.

Griesche, H. J., Barrientos-Velasco, C., Deneke, H., Hünerbein, A., Seifert, P., and Macke, A.: Low-level Arctic clouds: a blind zone in our knowledge of the radiation budget, Atmospheric Chemistry and Physics, 24, 597–612, https://doi.org/10.5194/acp-24-597-2024, 2024.

Hegerl, G. C.: Climate change is physics, Communications Earth & Environment, 3, 1–3, https://doi.org/10.1038/s43247-022-00342-8, publisher: Nature Publishing Group, 2022.

Hofer, S., Hahn, L. C., Shaw, J. K., McGraw, Z. S., Bruno, O., Hellmuth, F., Pietschnig, M., Mostue, I. A., David, R. O., Carlsen, T., and Storelvmo, T.: Realistic representation of mixed-phase clouds increases projected climate warming, Communications Earth & Environment, 5, 1–12, https://doi.org/10.1038/s43247-024-01524-2, publisher: Nature Publishing Group, 2024.

Illingworth, A. J., Hogan, R. J., O'Connor, E. J., Bouniol, D., Brooks, M. E., Delanoé, J., Donovan, D. P., Eastment, J. D., Gaussiat, N., Goddard, J. W. F., Haeffelin, M., Baltink, H. K., Krasnov, O. A., Pelon, J., Piriou, J.-M., Protat, A., Russchenberg, H. W. J., Seifert, A., Tompkins, A. M., van Zadelhoff, G.-J., Vinit, F., Willén, U., Wilson, D. R., and Wrench, C. L.: CloudnetContinuous Evaluation of Cloud Profiles in Seven Operational Models Using Ground-Based Observations, Bull. Amer. Meteor. Soc., 88, 883–898, https://doi.org/10.1175/BAMS-88-6-883, publisher: American Meteorological Society, 2007.

Jensen, M., Giangrande, S., Fairless, T., and Zhou, A.: Interpolated Sonde (INTERPOLATEDSONDE), Atmospheric Radiation Measurement (ARM) user facility, https://doi.org/10.5439/1095316, last access: 30 April, 2024.

Johnson, K., Giangrande, S., and Toto, T.: Active Remote Sensing of CLouds (ARSCL) product using Ka-band ARM Zenith Radars (ARSCLKAZR1KOLLIAS), Atmospheric Radiation Measurement (ARM) user facility, https://doi.org/10.5439/1393437, last access: 30 April, 2024.

JPL ENSO: El Niño Southern Oscillation index, Jet Propulsion Laboratory, California Institute of Technology, https://sealevel.jpl.nasa.gov/data/vital-signs/el-nino/, Last access 30 April 2025.

JPL PDO: Pacific Decadal Oscillation index, Jet Propulsion Laboratory, California Institute of Technology, https://sealevel.jpl.nasa.gov/data/vital-signs/pacific-decadal-oscillation, Last access 30 April 2025.

Kalesse-Los, H., Schimmel, W., Luke, E., and Seifert, P.: Evaluating cloud liquid detection against Cloudnet using cloud radar Doppler spectra in a pre-trained artificial neural network, Atmospheric Measurement Techniques, 15, 279–295, https://doi.org/10.5194/amt-15-279-2022, 2022.

Kodaira, T., Waseda, T., Nose, T., and Inoue, J.: Record high Pacific Arctic seawater temperatures and delayed sea ice advance in response to episodic atmospheric blocking, Scientific Reports, 10, 20 830, https://doi.org/10.1038/s41598-020-77488-y, number: 1 Publisher: Nature Publishing Group, 2020.

Korolev, A. and Milbrandt, J.: How are mixed-phase clouds mixed?, Geophysical Research Letters, 49, https://doi.org/10.1029/2022GL099578, e2022GL099578, 2022.

Lapere, R., Marelle, L., Rampal, P., Brodeau, L., Melsheimer, C., Spreen, G., and Thomas, J. L.: Modeling the contribution of leads to sea spray aerosol in the high Arctic, Atmospheric Chemistry and Physics, 24, 12 107–12 132, https://doi.org/10.5194/acp-24-12107-2024, 2024.

Li, X., Krueger, S. K., Strong, C., and Mace, G. G.: Relationship Between Wintertime Leads and Low Clouds in the Pan-Arctic, Journal of Geophysical Research: Atmospheres, 125, e2020JD032 595, https://doi.org/10.1029/2020JD032595, 2020a.

Li, X., Krueger, S. K., Strong, C., Mace, G. G., and Benson, S.: Midwinter Arctic leads form and dissipate low clouds, Nature Communications, 11, 206, https://doi.org/10.1038/s41467-019-14074-5, 2020b.

Lubin, D., Zou, X., Mülmenstädt, J., Vogelmann, A., Cadeddu, M., and Zhang, D.: Surface radiation trends at North Slope of Alaska influenced by large-scale circulation and atmospheric rivers, Atmospheric Chemistry and Physics, 26, 295–311, https://doi.org/10.5194/acp-26-295-2026, 2026.

Manaster, A., O'Dell, C. W., and Elsaesser, G.: Evaluation of Cloud Liquid Water Path Trends Using a Multidecadal Record of Passive Microwave Observations, https://doi.org/10.1175/JCLI-D-16-0399.1, section: Journal of Climate, 2017.

Mann, M. E., Steinman, B. A., and Miller, S. K.: Absence of internal multidecadal and interdecadal oscillations in climate model simulations, Nature Communications, 11, 49, https://doi.org/10.1038/s41467-019-13823-w, publisher: Nature Publishing Group, 2020.

Melsheimer, C. and Spreen, G.: AMSR-E ASI sea ice concentration data, Arctic, version 5.4 (NetCDF) (June 2002 - September 2011), PANGAEA, https://doi.org/10.1594/PANGAEA.899090, last acctess: 30 April 2024, 2019.

Morrison, H., de Boer, G., Feingold, G., Harrington, J., Shupe, M. D., and Sulia, K.: Resilience of persistent Arctic mixed-phase clouds, Nature Geosci, 5, 11–17, https://doi.org/10.1038/ngeo1332, number: 1 Publisher: Nature Publishing Group, 2012.

Nakanishi, M. and Michibata, T.: How Does Cloud Emissivity Feedback Affect Present and Future Arctic Warming?, Ocean-Land-Atmosphere Research, 4, 0089, https://doi.org/10.34133/olar.0089, publisher: American Association for the Advancement of Science, 2025.

NOAA AO: Artic Oscillation index, National Ocean and Atmospheric Administration, https://ftp.cpc.ncep.noaa.gov/cwlinks/norm.daily.ao.cdas.z1000.19500101_current.csv, Last access 30 April 2025.

Notz, D. and Community, S.: Arctic Sea Ice in CMIP6, Geophysical Research Letters, 47, e2019GL086 749, https://doi.org/10.1029/2019GL086749, _eprint: https://onlinelibrary.wiley.com/doi/pdf/10.1029/2019GL086749, 2020.

O'Connor, E.: Model data from Barrow from 1 November 2011 to 30 April 2025, ACTRIS Cloud remote sensing data centre unit (CLU), https://hdl.handle.net/21.12132/1.b1fac6f389b740e7, data is volatile and may be updated in the future. Last access 30 April, 2025.

Palm, S. P., Strey, S. T., Spinhirne, J., and Markus, T.: Influence of Arctic sea ice extent on polar cloud fraction and vertical structure and implications for regional climate, Journal of Geophysical Research: Atmospheres, 115, https://doi.org/10.1029/2010JD013900, _eprint: https://agupubs.onlinelibrary.wiley.com/doi/pdf/10.1029/2010JD013900, 2010.

Papakonstantinou-Presvelou, I., Sourdeval, O., and Quaas, J.: Strong Ocean/Sea-Ice Contrasts Observed in Satellite-Derived Ice Crystal Number Concentrations in Arctic Ice Boundary-Layer Clouds, Geophysical Research Letters, 49, e2022GL098 207, https://doi.org/10.1029/2022GL098207, _eprint: https://onlinelibrary.wiley.com/doi/pdf/10.1029/2022GL098207, 2022.

Pithan, F., Medeiros, B., and Mauritsen, T.: Mixed-phase clouds cause climate model biases in Arctic wintertime temperature inversions, Climate Dynamics, 43, 289–303, https://doi.org/10.1007/s00382-013-1964-9, 2014.

Rantanen, M., Karpechko, A. Y., Lipponen, A., Nordling, K., Hyvärinen, O., Ruosteenoja, K., Vihma, T., and Laaksonen, A.: The Arctic has warmed nearly four times faster than the globe since 1979, Communications Earth & Environment, 3, 1–10, https://doi.org/10.1038/s43247-022-00498-3, number: 1 Publisher: Nature Publishing Group, 2022.

Riihimaki, L., Zhang, D., and Gaustad, K.: Radiative Flux Analysis (RADFLUX1LONG), North Slope Alaska (NSA), Central Facility, Barrow AK (C1), Tech. rep., https://doi.org/10.5439/1395159, last access: 30 April, 2024.

Rogers, R. and Yau, M.: A Short Course in Clouds Physics, Pergamon Press, third edition edn., 1991.

Saavedra Garfias, P. and Kalesse-Los, H.: CloudnetTools.jl: A Julia package to apply Cloudnet to data from the ARM facility, https://doi.org/10.5281/zenodo.7245670, *in preparation*, 2022.

Saavedra Garfias, P. and Kalesse-Los, H.: Wintertime Arctic cloud properties coupled to sea ice leads during MOSAiC expedition, Harvard Dataverse, https://doi.org/10.7910/DVN/DZSUV7, 2023.

Saavedra Garfias, P. and Kalesse-Los, H.: Long-term statistical analysis of wintertime cloud thermodynamic phase and micro-physical properties in relation to sea ice condition at NSA Utqiaġvik site, ESS Open Archive, https://doi.org/10.22541/essoar.170516166.65463592/v1, 2024.

Saavedra Garfias, P., Kalesse-Los, H., von Albedyll, L., Griesche, H., and Spreen, G.: Asymmetries in cloud microphysical properties ascribed to sea ice leads via water vapour transport in the central Arctic, Atmospheric Chemistry and Physics, 23, 14 521–14 546, https://doi.org/10.5194/acp-23-14521-2023, 2023.

Saavedra Garfias, P., Kalesse-Los, H., and Ebell, K.: Estimation of wintertime cloud radiative effects in the Western Arctic, a function of cloud-moisture-coupling and sea ice conditions, AIP Conference Proceedings, 2988, 070 008, https://doi.org/10.1063/5.0182751, 2024.

Schäfer, B., David, R. O., Hodnebrog, Ø., and Storelvmo, T.: Response of an Arctic Mixed-Phase Cloud to Ice-Nucleating Particle Perturbations and Warming, Geophysical Research Letters, 52, e2024GL114 467, https://doi.org/https://doi.org/10.1029/2024GL114467, e2024GL114467 2024GL114467, 2025.

Schemann, V. and Ebell, K.: Simulation of mixed-phase clouds with the ICON large-eddy model in the complex Arctic environment around Ny-Ålesund, Atmospheric Chemistry and Physics, 20, 475–485, https://doi.org/https://doi.org/10.5194/acp-20-475-2020, publisher: Copernicus GmbH, 2020.

Schimmel, W., Kalesse-Los, H., Maahn, M., Vogl, T., Foth, A., Garfias, P. S., and Seifert, P.: Identifying cloud droplets beyond lidar attenuation from vertically pointing cloud radar observations us ing artificial neural networks, Atmospheric Measurement Techniques, 15, 5343–5366, https://doi.org/10.5194/amt-15-5343-2022, 2022.

Serreze, M. C. and Barry, R. G.: Processes and impacts of Arctic amplification: A research synthesis, Global and Planetary Change, 77, 85–96, https://doi.org/10.1016/j.gloplacha.2011.03.004, 2011.

Serreze, M. C. and Barry, R. G.: The Arctic climate system, Cambridge atmospheric and space science series, Cambridge university press, New York, 2nd ed edn., 2014.

Serreze, M. C. and Francis, J. A.: The Arctic Amplification Debate, Climatic Change, 76, 241–264, https://doi.org/10.1007/s10584-005-9017-y, 2006.

Serreze, M. C., Box, J. E., Barry, R. G., and Walsh, J. E.: Characteristics of Arctic synoptic activity, 1952-1989, Meteorology and Atmospheric Physics, 51, 147–164, https://doi.org/10.1007/BF01030491, 1993.

Shi, Y., Howie, J., Goldberger, L., and Morris, V.: Infrared Thermometer (GNDIRT), North Slope Alaska (NSA), Central Facility, Barrow AK (C1), https://doi.org/10.5439/1366509, last access: 30 April, 2024.

Shupe, M. D. and Intrieri, J. M.: Cloud Radiative Forcing of the Arctic Surface: The Influence of Cloud Properties, Surface Albedo, and Solar Zenith Angle, Journal of Climate, 17, 616–628, https://doi.org/10.1175/1520-0442(2004)017<0616:CRFOTA>2.0.CO;2, publisher: American Meteorological Society Section: Journal of Climate, 2004.

Shupe, M. D., Matrosov, S. Y., and Uttal, T.: Arctic mixed-phase cloud properties derived from surface-based sensors at SHEBA, J. Atmos. Sci., 63, 697–711, 2006.

Shupe, M. D., Walden, V. P., Eloranta, E., Uttal, T., Campbell, J. R., Starkweather, S. M., and Shiobara, M.: Clouds at Arctic Atmospheric Observatories. Part I: Occurrence and Macrophysical Properties, Journal of Applied Meteorology and Climatology, 50, 626 – 644, https://doi.org/10.1175/2010JAMC2467.1, 2011.

Shupe, M. D., Rex, M., Blomquist, B., Persson, P. O. G., Schmale, J., Uttal, T., Althausen, D., Angot, H., and et al.: Overview of the MOSAiC expedition—Atmosphere, Elementa: Science of the Anthropocene, 10, 00 060, https://doi.org/10.1525/elementa.2021.00060, 2022.

Spiess, A.-N. and Neumeyer, N.: An evaluation of R2 as an inadequate measure for nonlinear models in pharmacological and biochemical research: a Monte Carlo approach, BMC Pharmacology, 10, 6, https://doi.org/10.1186/1471-2210-10-6, 2010.

Spreen, G., Kaleschke, L., and Heygster, G.: Sea ice remote sensing using AMSR-E 89-GHz channels, Journal of Geophysical Research: Oceans, 113, https://doi.org/https://doi.org/10.1029/2005JC003384, 2008.

Tan, I. and Storelvmo, T.: Evidence of Strong Contributions From Mixed-Phase Clouds to Arctic Climate Change, Geophysical Research Letters, 46, 2894–2902, https://doi.org/https://doi.org/10.1029/2018GL081871, 2019.

Tan, I., Sotiropoulou, G., Taylor, P. C., Zamora, L., and Wendisch, M.: A Review of the Factors Influencing Arctic Mixed-Phase Clouds: Progress and Outlook, chap. 5, pp. 103–132, American Geophysical Union (AGU), https://doi.org/https://doi.org/10.1002/9781119700357.ch5, 2023.

Tan, I., Zhou, C., Lamy, A., and Stauffer, C. L.: Moderate climate sensitivity due to opposing mixed-phase cloud feedbacks, npj Climate and Atmospheric Science, 8, 1–6, https://doi.org/10.1038/s41612-025-00948-7, publisher: Nature Publishing Group, 2025.

Timmermann, A., An, S.-I., Kug, J.-S., Jin, F.-F., Cai, W., Capotondi, A., and et. alli: El Niño–Southern Oscillation complexity, Nature, 559, 535–545, https://doi.org/10.1038/s41586-018-0252-6, publisher: Nature Publishing Group, 2018.

Tobo, Y., Adachi, K., Kawai, K., Matsui, H., Ohata, S., Oshima, N., Kondo, Y., Hermansen, O., Uchida, M., Inoue, J., and Koike, M.: Surface warming in Svalbard may have led to increases in highly active ice-nucleating particles, Communications Earth & Environment, 5, 516, https://doi.org/10.1038/s43247-024-01677-0, publisher: Nature Publishing Group, 2024.

Toto, T. and Giangrande, S.: Ka-Band ARM Zenith RADAR (KAZR) CF-Radial, Corrected VAP (KAZRCFRCORGE), https://doi.org/10.5439/1560129, last access: 30 April, 2024.

Tukiainen, S., O'Connor, E., and Korpinen, A.: CloudnetPy: A Python package for processing cloud remote sensing data, Journal of Open Source Software, 5, 2123, https://doi.org/10.21105/joss.02123, 2020.

von Albedyll, L., Hendricks, S., Hutter, N., Murashkin, D., Kaleschke, L., Willmes, S., Thielke, L., Tian-Kunze, X., Spreen, G., and Haas, C.: Lead fractions from SAR-derived sea ice divergence during MOSAiC, The Cryosphere, 18, 1259–1285, https://doi.org/10.5194/tc-18-1259-2024, 2024.

Wendisch, M., Brückner, M., Crewell, S., Ehrlich, A., Notholt, J., Lüpkes, C., Macke, A., Burrows, J. P., Rinke, A., Quaas, J., Maturilli, M., Schemann, V., Shupe, M. D., and et al.: Atmospheric and Surface Processes, and Feedback Mechanisms Determining Arctic Amplification: A Review of First Results and Prospects of the (AC)3 Project, Bulletin of the American Meteorological Society, 104, E208 – E242, https://doi.org/10.1175/BAMS-D-21-0218.1, 2023.

Zhang, D.: MWR Retrievals (MWRRET1LILJCLOU), Atmospheric Radiation Measurement (ARM) user facility, https://doi.org/10.5439/1027369, last access: 30 April, 2024.

Zhang, D., Morris, V., and Ermold, B.: Ceilometer (CEIL10M), North Slope Alaska (NSA), Central Facility, Barrow AK (C1), https://doi.org/10.5439/1497398, last access: 30 April, 2024.

Zhang, P., Chen, G., Ting, M., Ruby Leung, L., Guan, B., and Li, L.: More frequent atmospheric rivers slow the seasonal recovery of Arctic sea ice, Nature Climate Change, 13, 266–273, https://doi.org/10.1038/s41558-023-01599-3, number: 3 Publisher: Nature Publishing Group, 2023.

Zhang, Z. and Moore, J.: New significance test methods for Fourier analysis of geophysical time series, Nonlinear Processes in Geophysics, 18, 643–652, https://doi.org/10.5194/npg-18-643-2011, publisher: Copernicus GmbH, 2011.

Zhong, W., Shi, Q., Yang, Q., Liu, J., and Yang, S.: Wintertime Arctic Sea-Ice Decline Related to Multi-Year La Niña Events, Advances in Atmospheric Sciences, 41, 1680–1690, https://doi.org/10.1007/s00376-024-3194-y, 2024.